CHAPTER 10

The Seismic Source: Kinematics

In Section 2.5 and Chapter 3, we studied seismic sources so that we could begin to determine what aspects of the theory of wave propagation are needed in seismology. Having completed a study of wave propagation in Chapters 4–9, we return here to a more thorough examination of seismic sources. Of all the various types of source that can generate seismic waves (explosions, rapid phase transformations, etc.), the principal source we shall study is that involving a surface (the fault plane) across which shearing motions develop. In Section 3.1, we showed that if the displacement discontinuity across a fault surface is a known function of time and position on the fault, then motions throughout the medium are completely determined. This result provides the basis of the present chapter, in which we shall characterize what may be learned from far-field and near-field observations about the kinematics of motion at an earthquake source.

To understand the physical processes actually occurring in the source region, one must study stress-dependent material properties such as the way in which material failure nucleates and spreads (e.g., over a fault plane), rapidly relieving stresses that had slowly risen (due to long-term tectonic processes) to exceed the strength of material in the source region. This is a dynamic problem, and a very difficult one, which we take up in the next chapter. As we develop now the simpler problem of fault kinematics, we are guided to some extent by the constraint that faulting is a process of failure in shear.

Our starting point is the representation theorem (equation (3.2)) of Chapter 3. Neglecting body forces and stress discontinuities, recall that the elastic displacement $\mathbf{u}$ caused by a displacement discontinuity $[\mathbf{u}(\xi, \tau)]$ across an internal surface Σ has the components

$$u_i(\mathbf{x}, t) = \int_{-\infty}^{\infty} d\tau \iint_{\Sigma} [u_j(\xi, \tau)] c_{jkpq} G_{ip,q}(\mathbf{x}, t; \xi, \tau) \nu_k \, d\Sigma(\xi), \qquad (10.1)$$

where c_{jkpq} are the elastic moduli defined in equation (2.18); $G_{ip}(\mathbf{x}, t : \xi, \tau)$ is the Green function defined in Section 2.4; ν is the normal to Σ as shown in Figure 3.1; and $G_{ip,q}(\mathbf{x}, t : \xi, \tau)$ is the derivative of G_{ip} with respect to ξ_q. In a homogeneous, isotropic, unbounded

medium, the Green function can be stated explicitly. Thus, using (2.37) and (4.23), with body force taken as a unit impulse, it follows that

$$\begin{aligned} G_{ip}(\mathbf{x},t;\xi,\tau) = {} & \frac{1}{4\pi\rho}(3\gamma_i\gamma_p - \delta_{ip})\frac{1}{r^3}\int_{r/\alpha}^{r/\beta} t'\,\delta(t-\tau-t')\,dt' \\ & + \frac{1}{4\pi\rho\alpha^2}\gamma_i\gamma_p\frac{1}{r}\delta\left(t-\tau-\frac{r}{\alpha}\right) \\ & - \frac{1}{4\pi\rho\beta^2}(\gamma_i\gamma_p - \delta_{ip})\frac{1}{r}\delta\left(t-\tau-\frac{r}{\beta}\right), \end{aligned} \tag{10.2}$$

where γ is the unit vector from the source point ξ to the receiver point $\mathbf{x}$, and $r = |\mathbf{x} - \xi|$ is the distance between those two points.

10.1 Kinematics of an Earthquake as Seen at Far Field

We shall obtain formulas for the displacement waveforms of P- and S-waves in the far field for faulting in a homogeneous medium. After outlining some general properties of these waveforms, we shall look in particular at their low-frequency component. Specializing next to the case of unidirectional propagation, we shall study waveforms due to a source characterized by five parameters: the fault length; the fault width; the rupture velocity; the final offset; and the "rise time," which characterizes the time taken for the offset, at a particular point on the fault, to reach its final value. This simple five-parameter characterization is often adequate to interpret the waves leaving a finite source. Where a more detailed description of the fault motions is required, we can separately study different stages of the faulting process such as nucleation of motion, the spreading of rupture, and the stopping of motion. We describe several examples of these stages and conclude the analysis of far-field waveforms with an examination of their intermediate-frequency and high-frequency content.

10.1.1 FAR-FIELD DISPLACEMENT WAVEFORMS OBSERVED IN A HOMOGENEOUS, ISOTROPIC, UNBOUNDED MEDIUM

We choose to work with a homogeneous, isotropic, unbounded medium in order to minimize the complication of path effects.

If the receiver position $\mathbf{x}$ is sufficiently far from all points ξ on the fault surface Σ, then only the far-field terms in the Green function (10.2) are significant. From (10.1), after carrying out the integral with respect to τ, we obtain the far-field displacement

$$\begin{aligned} u_i(\mathbf{x},t) = {} & -\frac{1}{4\pi\rho\alpha^2}\frac{\partial}{\partial x_q}\iint_\Sigma c_{jkpq}\frac{\gamma_i\gamma_p}{r}\left[u_j\left(\xi,t-\frac{r}{\alpha}\right)\right]\nu_k\,d\Sigma \\ & + \frac{1}{4\pi\rho\beta^2}\frac{\partial}{\partial x_q}\iint_\Sigma c_{jkpq}\left(\frac{\gamma_i\gamma_p - \delta_{ip}}{r}\right)\left[u_j\left(\xi,t-\frac{r}{\beta}\right)\right]\nu_k\,d\Sigma, \end{aligned} \tag{10.3}$$

in which we have used the relation $\partial/\partial\xi_q = -\partial/\partial x_q$, valid for operations on quantities such as γ and r, which are dependent only on the difference between $\mathbf{x}$ and ξ. Carrying out the differentiation with respect to x_q, noting that $\partial r/\partial x_q$ is merely γ_q, and ignoring all terms that attenuate with distance more rapidly than r^{-1}, we obtain

$$\begin{aligned}\text{far-field of } u_i(\mathbf{x},t) = &\iint_\Sigma \frac{c_{jkpq}}{4\pi\rho\alpha^3 r}\gamma_i\gamma_p\left[\dot{u}_j\left(\xi, t-\frac{r}{\alpha}\right)\right]\gamma_q\nu_k\, d\Sigma \\ &- \iint_\Sigma \frac{c_{jkpq}}{4\pi\rho\beta^3 r}(\gamma_i\gamma_p - \delta_{ip})\left[\dot{u}_j\left(\xi, t-\frac{r}{\beta}\right)\right]\gamma_q\nu_k\, d\Sigma.\end{aligned} \tag{10.4}$$

Obviously, the first term corresponds to P-waves and the second to S-waves.

If the station is far enough away, as compared to the linear dimension of fault surface Σ, we can safely assume that the distance r and direction cosine γ_i are approximately constant, independent of ξ, and that such slowly varying factors can be taken outside the integral. For simplicity, we shall further assume that the fault surface Σ is a plane and that the direction of the displacement discontinuity is the same everywhere on the fault. We write

$$[u_j(\xi,t)] = n_j \cdot \Delta u(\xi,t), \tag{10.5}$$

where Δu is a scalar function, which we shall call the "source function," or the "slip function" in the case of a shear fault. Under these assumptions, equation (10.4) reduces to

$$\begin{aligned}\text{far-field of } u_i(\mathbf{x},t) = &\frac{\gamma_i}{4\pi\rho\alpha^3 r_0}\cdot c_{jkpq}\gamma_p\gamma_q\nu_k n_j \cdot \iint_\Sigma \Delta\dot{u}\left(\xi, t-\frac{r}{\alpha}\right) d\Sigma \\ &+ \frac{\delta_{ip}-\gamma_i\gamma_p}{4\pi\rho\beta^3 r_0}\cdot c_{jkpq}\gamma_q\nu_k n_j \cdot \iint_\Sigma \Delta\dot{u}\left(\xi, t-\frac{r}{\beta}\right) d\Sigma.\end{aligned} \tag{10.6}$$

In general, $\Delta\dot{u}$ can vary rapidly with time and space—so the retarded times in the integrands of (10.6) must include the variation of r with ξ. The overall amplitude factor r_0^{-1} is based on the distance r_0 to the receiver from a reference point on the fault.

The above equation permits a remarkably simple exposition of far-field displacement due to P- and S-waves from an earthquake source. Since $\gamma_i\gamma_i = 1$ and $\gamma_i(\delta_{ip} - \gamma_i\gamma_p) = 0$, we see immediately that the particle motion of P-waves is parallel to γ, and that of S-waves is perpendicular to γ. Wave amplitudes attenuate with distance as r_0^{-1}, and are inversely proportional to the cube of their propagation velocities. Since other factors are comparable between them, the S-wave amplitude is roughly α^3/β^3 (~ 5) times larger than the P-wave amplitude.

The factor $(c_{jkpq}\gamma_p\gamma_q\nu_k n_j)$ represents the radiation pattern of P-waves, determined by the orientation of the fault plane (ν_k), the direction of the displacement discontinuity (n_j), and the direction to the station (γ_p) from the fault. Similarly, taking γ' and γ'' as orthogonal unit vectors in the plane perpendicular to γ, the radiation of S-waves is described by their amplitude $(c_{jkpq}\gamma'_p\gamma_q\nu_k n_j)$ in the γ'-direction and $(c_{jkpq}\gamma''_p\gamma_q\nu_k n_j)$ in the γ''-direction.

Relative amplitudes between the two directions determine the polarization angle for S-waves, which is sometimes used (in addition to the first motion for P-waves) for determining fault-plane solutions.

Finally, the shapes of the displacement waveforms of P- and S-waves in equation (10.6) are described by the only terms exhibiting a time dependence. These waveform shapes are therefore simple integrals of the form

$$\Omega(\mathbf{x}, t) = \iint_{\Sigma} \Delta\dot{u}\left(\xi, t - \frac{|\mathbf{x} - \xi|}{c}\right) d\Sigma(\xi), \tag{10.7}$$

where c is the velocity of wave propagation (either α or β).

10.1.2 FAR-FIELD DISPLACEMENT WAVEFORMS FOR INHOMOGENEOUS ISOTROPIC MEDIA, USING THE GEOMETRICAL-SPREADING APPROXIMATION

In Chapter 4, equations (4.84)–(4.86), we obtained the far-field displacement at $\mathbf{x}$ under the assumption that the whole fault (with area A) was acting effectively as a point source. This is the case when wavelengths of interest are much longer than the fault dimensions, but are much shorter than the distance from source region to receiver. But throughout all of this Section 10.1 we are interested in the more general case in which wavelengths may be comparable with (and possibly less than) the fault dimensions, so that there can be interference between waves radiated from different parts of the fault surface. Making an analogy with electromagnetic wave generation, we are thinking here of the waves from a finite antenna, whose linear dimensions may be longer than the radiated wavelength.

Note that an alternative way to obtain the far-field displacement waveform (10.4) is to integrate the effect of each area element $d\Sigma$ regarded as a point source, using (4.84) for the P-waves and (4.85) for S-waves, but making allowance for different travel times to $\mathbf{x}$ from different parts of the fault surface. For example, for P-waves, using $[\dot{\mathbf{u}}]\,d\Sigma$ now instead of $\bar{\dot{\mathbf{u}}}A$, we find from (4.84) that

$$\text{far-field } P\text{-wave of } u_i(\mathbf{x}, t) = \frac{1}{4\pi\rho\alpha^3} \iint_{\Sigma} 2\mu \frac{\gamma_i \gamma_j}{r} \left[\dot{u}_j\left(\xi, t - \frac{|\mathbf{x} - \xi|}{\alpha}\right)\right] \gamma_k \nu_k \, d\Sigma(\xi), \tag{10.8}$$

which is just the same as the P-wave component in (10.4), since $c_{jkpq}[\dot{u}_j]\gamma_q \nu_k = 2\mu\gamma_j[\dot{u}_j]\gamma_k\nu_k$ for slip in isotropic media.

The virtue of this latter approach is that it can so easily be extended to inhomogeneous media, since in Chapter 4 we identified the far-field approximation with the geometrical-spreading approximation, and in equations (4.93)–(4.95) we gave what can be regarded as

the integrand of the integral we now need for a finite fault surface. For inhomogeneous media, then, the equation that generalizes the P-wave component of (10.6) is

$$\text{far-field } P\text{-wave of } \mathbf{u}(\mathbf{x}, t)$$
$$= \frac{\mathcal{F}^P \mu(\xi_0)\, \mathbf{l}}{4\pi \sqrt{\rho(\xi_0)\rho(\mathbf{x})\alpha(\xi_0)\alpha(\mathbf{x})}\, \alpha^2(\xi_0)\mathcal{R}^P(\mathbf{x}, \xi_0)} \iint_\Sigma \Delta\dot{u}(\xi, t - T^P(\mathbf{x}, \xi))\, d\Sigma, \tag{10.9}$$

in which $\mathbf{l}$ (the direction at $\mathbf{x}$ of the ray from the fault), $\mathcal{F}^P$ (the radiation pattern), and $\mathcal{R}^P$ (the geometrical spreading factor) are evaluated for some reference point ξ_0 on Σ. Formulas similar to (10.9) but for the waveforms of SV and SH can immediately be written down from (4.94) and (4.95).

10.1.3 GENERAL PROPERTIES OF DISPLACEMENT WAVEFORMS IN THE FAR FIELD

For convenience in presentation, we shall continue to use homogenous media for development of the theory, giving in Box 10.2 an example of how our source theory can be merged with wave-propagation theory for realistic media.

Taking the origin of coordinates at a reference point on the fault, the distance r between the surface element $d\Sigma$ and the receiver point $\mathbf{x}$ can be written as

$$\begin{aligned} r = |\mathbf{x} - \xi| &= r_0 \sqrt{1 + \frac{|\xi|^2}{r_0^2} - \frac{2(\xi \cdot \gamma)}{r_0}} \\ &= r_0 \left\{ 1 + \frac{1}{2}\left[\frac{|\xi|^2}{r_0^2} - \frac{2(\xi \cdot \gamma)}{r_0} \right] - \frac{1}{8}\left[\quad \right]^2 \cdots \right\} \\ &= r_0 - (\xi \cdot \gamma) + \frac{1}{2}\frac{|\xi|^2}{r_0} - \frac{(\xi \cdot \gamma)^2}{2r_0} + \cdots, \end{aligned} \tag{10.10}$$

where r_0 is the distance to the receiver from the origin, $r_0 = |\mathbf{x}|$, γ is the unit vector pointing to the receiver, and ξ is the location vector of $d\Sigma$ measured from the origin (Fig. 10.1).

For r_0 large compared with the linear dimension of Σ, we may approximate equation (10.10) by

$$r \sim r_0 - (\xi \cdot \gamma). \tag{10.11}$$

The error δr in path length due to this approximation may be estimated by the largest terms neglected in the series expansion in equation (10.10):

$$\delta r = \frac{1}{2r_0}[|\xi|^2 - (\xi \cdot \gamma)^2].$$

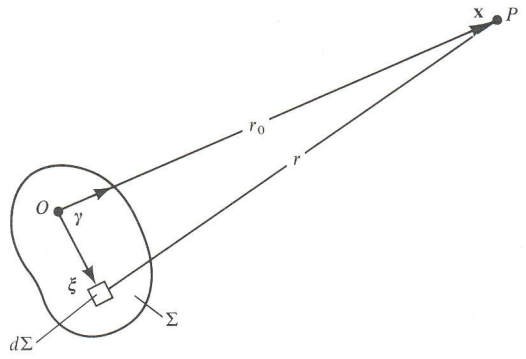

FIGURE **10.1**
The origin of coordinates is taken on a finite fault surface.

If this error is equal to or greater than a quarter wavelength, $\lambda/4$, a serious error will be introduced in the result of integration. Therefore, the approximation by equation (10.11) is justified only for

$$\frac{1}{2r_0}\left[|\xi|^2 - (\xi \cdot \gamma)^2\right] \ll \frac{\lambda}{4}$$

or, conservatively,

$$L^2 \ll \tfrac{1}{2}\lambda r_0, \tag{10.12}$$

where L is the maximum of $|\xi|$ on Σ. This is the same as the condition to be satisfied for the region of Fraunhofer diffraction in optics. For comparison, note that the condition we assumed in Chapter 4, in which the whole fault was regarded as a point source, amounted to $L \ll \gamma$, which is a much more restrictive condition on the applicable frequency range than (10.12). Under condition (10.12), we can rewrite the displacement waveform given in equation (10.7) as

$$\Omega(\mathbf{x}, t) = \Omega(\gamma, t) = \iint_\Sigma \Delta\dot{u}\left[\xi, t - \frac{r_0 - (\xi \cdot \gamma)}{c}\right] d\Sigma. \tag{10.13}$$

Note that the far-field pulse shape depends more directly on γ than on $\mathbf{x}$, since it is position on the focal sphere which governs this pulse shape, and many positions $\mathbf{x}$ have the same value of γ.

Taking the Fourier transform of the above equation with respect to t, we get

$$\begin{aligned}\Omega(\mathbf{x}, \omega) = \Omega(\gamma, \omega) &= \iint_\Sigma \Delta\dot{u}(\xi, \omega)\ \exp\left\{\frac{i\omega\left[r_0 - (\xi \cdot \gamma)\right]}{c}\right\} d\Sigma \\ &= \exp\left(\frac{i\omega r_0}{c}\right) \iint_\Sigma \Delta\dot{u}(\xi, \omega)\ \exp\left[\frac{-i\omega(\xi \cdot \gamma)}{c}\right] d\Sigma\end{aligned} \tag{10.14}$$

This shows that the Fourier transform $\Omega(\gamma, \omega)$ of the observed displacement waveform with phase correction for the delay $\omega r_0/c$ due to propagation can be expressed as a superposition of plane waves of the type $\exp[-i\omega(\xi \cdot \gamma)/c]$. Specifically,

$$\Omega(\gamma, \omega)e^{-i\omega r_0/c} = \iint_\Sigma \Delta\dot{u}(\xi, \omega)\ \exp\left[-i\omega(\xi \cdot \gamma)/c\right]\ d\Sigma. \tag{10.15}$$

This right-hand side has the form of a double Fourier transform in space. It is given by $\iint_\Sigma\ \Delta\dot{u}(\xi, \omega)\ \exp[-i(\xi \cdot \mathbf{k})]\ d\Sigma = f(\mathbf{k})$. If the transform were known for all $\mathbf{k}$ in wavenumber space, we could invert the double integral and determine $\Delta\dot{u}(\xi, \omega)$ completely, as a function of ξ, from far-field observations. Unfortunately, (10.15) shows that the two-dimensional transform is known not for all $\mathbf{k}$, but only for the projection of $\omega\gamma/c$ on Σ (we are assuming that Σ is flat, so that ξ lies in the plane of Σ). The range of $\mathbf{k}$ we can recover from far-field observations is therefore restricted to $\mathbf{k}$ parallel to Σ, and, since γ is a unit vector, $|\mathbf{k}| \leq \omega/c$. It follows that we cannot find details of the seismic source with scale lengths shorter than the shortest wavelength observed. The phase velocity along the plane Σ of the plane waves in (10.15) is $\omega/|\mathbf{k}|$, and $c \leq \omega/|\mathbf{k}|$. So the underlying reason for not being able to elucidate short wavelength features of the source is that the only waves which can radiate to the far field are those whose phase velocity (along the plane Σ) is greater than the medium velocity c. The waves with phase velocity smaller than c are inhomogeneous waves trapped near Σ, and we investigate them further in Sections 10.2.3 and 10.2.4. Here, we note that for a complete recovery of the source function $\Delta u(\xi, t)$, we need observations at near field.

10.1.4 BEHAVIOR OF THE SEISMIC SPECTRUM AT LOW FREQUENCIES

As the frequency ω approaches zero, the Fourier transform $\Omega(\mathbf{x}, \omega)$ of the far-field displacement waveform, given in (10.14), approaches a constant value:

$$\Omega(\mathbf{x}, \omega \to 0) = \iint_\Sigma \Delta\dot{u}(\xi, \omega \to 0)\ d\Sigma.$$

Since

$$\Delta\dot{u}(\xi, \omega) = \int \Delta\dot{u}(\xi, t)\ \exp(i\omega t)\ dt$$

and also

$$\Delta\dot{u}(\xi, \omega \to 0) = \int \Delta\dot{u}(\xi, t)\ dt = \Delta u(\xi, t \to \infty),$$

we have

$$\Omega(\mathbf{x}, \omega \to 0) = \iint_\Sigma \Delta u(\xi, t \to \infty)\ d\Sigma. \tag{10.16}$$

Thus $\Omega(\mathbf{x}, \omega \to 0)$ in the limit is the integral of the final slip over the fault area—which is independent of γ, since the effect of the radiation pattern has been accounted for in a separate factor (see (10.6)). In other words, the spectrum (absolute value of Fourier transform) of the far-field displacement waveform tends to a constant at low frequencies, whose height is proportional to the seismic moment defined in equation (3.16). We leave it as Problem 10.5 to show that the spectrum is flat at the origin. This result is true for any $\Delta u(\xi, t)$ provided the final offset is the same, and the spectrum at low frequencies is independent of details of the process by which the final offset is acquired on the fault plane.

If we make an additional assumption that the fault-slip velocity never reverses its direction (i.e., that $\Delta \dot{u}$ does not change sign during an earthquake—a reasonable assumption if there is significant friction still operating on the fault plane at the time when $\Delta \dot{u}$ returns to zero, so that no further slip takes place), then, from equation (10.13), we find that $\Omega(\mathbf{x}, t)$ will have the same sign for all t. In that case, the Fourier transform $\Omega(\mathbf{x}, \omega)$ is not only flat but takes its maximum value at $\omega = 0$, and we say the source spectrum has no overshoot. This result, which is again independent of the details of faulting, has been pointed out by Savage (1972), Molnar, Jacob, and McCamy (1973), and Randall (1973) in a controversy triggered by Archambeau (1968) on the low-frequency behavior of the seismic spectrum of earthquake faulting. In contrast, the source spectrum of an explosion can have a prominent overshoot.

If the area of fault surface Σ is infinitesimally small and if the slip $\Delta u(\xi, t)$ varies as a step function in time, then we find from (10.13) or (4.84) that the far-field waveform is a delta function and hence that the spectrum is flat for the whole frequency range. Therefore, we may say that for low frequencies where the spectrum is flat, the seismic source is equivalent to a point source with a step-function slip. This simple source has been extensively used in the single-station method of determining phase velocities for Love and Rayleigh waves from relatively small earthquakes. Weidner (1972) compared the results obtained by the single-station method with those by the two-station method for North Atlantic paths and found that the step-function assumption was correct within a phase error of less than about 0.02–0.1 cycle for periods of 20–80 s and for earthquakes with magnitude 6 or less. The same assumption was also used successfully in the determination of the focal depth of earthquakes with magnitude less than about 6, using the amplitude (Tsai and Aki, 1971) and the phase (Weidner and Aki, 1973) of Rayleigh waves. The step-function assumption using free-oscillation data in the period range 150–1200 s is supported by Mendiguren (1972) and Russakof *et al.* (1997) for a deep earthquake in 1970 in Colombia. A summary of measurements on seismic moment and fault area was given by Kanamori and Anderson (1975) for many earthquakes of various magnitudes.

10.1.5 A FAULT MODEL WITH UNIDIRECTIONAL PROPAGATION

As shown in the preceding section, observed waveforms in the far field alone cannot uniquely determine the source function $\Delta u(\xi, t)$. It is therefore useful to establish a minimum set of source parameters that can adequately describe the source function. Limited observations in the far field can then be effectively used to determine these parameters.

Let us first describe the fault plane as a rectangle with length L and width W. The rupture initiates at one end of the fault and propagates along the length L with velocity v.

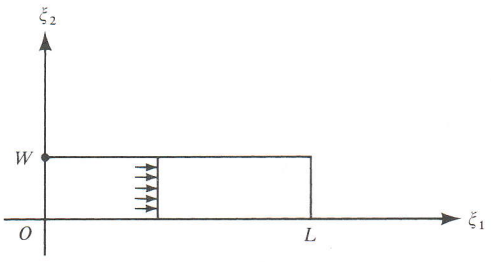

(a)

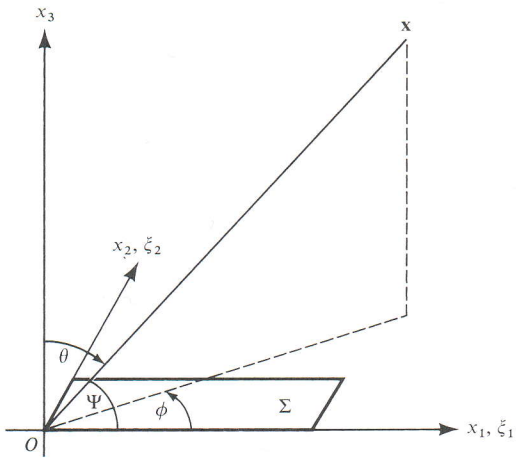

(b)

FIGURE **10.2**
Unidirectional faulting on a rectangular fault. (**a**) The fault plane. (**b**) Direction $\theta = 0$ is normal to the fault plane, and $\Psi = 0$ is the direction of rupture propagation.

Setting the coordinate system (ξ_1, ξ_2) parallel to the length and width of the fault plane as shown in Figure 10.2, we specify the rupture propagation by

$$\begin{aligned} \Delta u(\boldsymbol{\xi}, t) &= f(t - \xi_1/v) \qquad \text{if } 0 < \xi_1 < L \quad \text{and} \quad 0 < \xi_2 < W, \\ &= 0 \qquad\qquad\quad \text{if } \xi_1 < 0 \text{ or } \xi_1 > L, \quad \text{or} \quad \xi_2 < 0 \text{ or } \xi_2 > W. \end{aligned} \tag{10.17}$$

Putting this into equation (10.13), we get

$$\Omega(\mathbf{x}, t) = \int_0^W \int_0^L \dot{f}\left(t - \frac{r_0}{c} - \frac{\xi_1}{v} + \frac{\xi_1\gamma_1 + \xi_2\gamma_2}{c}\right) d\xi_1\, d\xi_2. \tag{10.18}$$

Assuming that W and $\xi_2\gamma_2$ are small, and taking Ψ as the angle between the direction to the receiver and the direction of rupture propagation, we can rewrite equation (10.18) as

$$\Omega(\mathbf{x}, t) = W \int_0^L \dot{f}\left[t - \frac{r_0}{c} - \xi_1\left(\frac{1}{v} - \frac{\cos\Psi}{c}\right)\right] d\xi_1. \tag{10.19}$$

Since this integrand ranges from $\dot{f}(t - r_0/c)$ to $\dot{f}(t - r_0/c - L[1/v - (\cos\Psi)/c])$, $\Omega(\mathbf{x}, t)$ given by (10.19) is proportional to a moving average of $\dot{f}(t - r_0/c)$ taken over a time interval

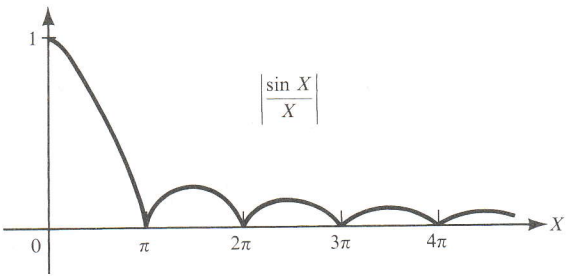

FIGURE **10.3**
The factor $|X^{-1} \sin X|$ in the spectrum of an observed pulse shape can be thought of in the time domain as convolution with a box function of temporal duration $L(1/v - c^{-1} \cos \Psi) = L[1/v - c^{-1}(\sin \theta \cos \phi)]$. This is the *apparent* duration of rupture, as detected by receivers along the direction (θ, ϕ), for rupture speed v and wave-propagation speed c.

with duration $L[1/v - (\cos \Psi)/c]$. Noting that $\dot{f}(t - r_0/c)$ is the far-field displacement waveform expected for an infinitesimally small fault, we see that rupture propagation over a finite fault length has a smoothing effect on the waveform.

To find this effect on the spectrum, we take the Fourier transform of (10.7). Writing the Fourier transform of $f(t)$ as $f(\omega)$, we get

$$\begin{aligned} \Omega(\mathbf{x}, \omega) &= -i\omega W f(\omega) e^{i\omega r_0/c} \int_0^L \exp\left[i\omega\xi_1 \left(\frac{1}{v} - \frac{\cos \Psi}{c}\right)\right] d\xi_1 \\ &= \omega f(\omega) W L \frac{\sin X}{X} \exp\left[i\left(\frac{\omega r_0}{c} - \frac{\pi}{2} + X\right)\right], \end{aligned} \tag{10.20}$$

where $X = (\omega L/2)[1/v - (\cos \Psi)/c]$. The effect of the finiteness of the fault on the amplitude spectrum is expressed by $X^{-1} \sin X$, which is depicted in Figure 10.3. This effect, first discussed by Ben-Menahem (1961), produces nodes at $X = \pi, 2\pi, \ldots$. The first node corresponds to the period $2\pi/\omega = L[1/v - (\cos \Psi)/c]$. An example of observed spectral nodes is shown in Figure 10.4 for Love waves from the Parkfield earthquake of 1966 June, observed at Berkeley, California (Filson and McEvilly, 1967). The first node at $T = 22.5$ s is explained by the rupture velocity of 2.2 km/s, the fault length of about 30 km, and $\cos \Psi$ of about 1.

For higher frequencies, the envelope of $X^{-1} \sin X$ is proportional to ω^{-1}. This smoothing effect is weakest in the direction of rupture propagation ($\Psi = 0$) and strongest in the opposite direction ($\Psi = \pi$). As a result, we observe more high-frequency waves at $\Psi = 0$ than at $\Psi = \pi$.

Two additional source parameters are needed to complete the unidirectional rectangular fault model. They are the final slip D and the rise time T characterizing the slip function $f(t)$. Haskell (1964) used a ramp function

$$\begin{aligned} f(t) &= 0 \qquad && t < 0, \\ &= Dt/T \qquad && 0 < t < T, \\ &= D \qquad && T < t, \end{aligned} \tag{10.21}$$

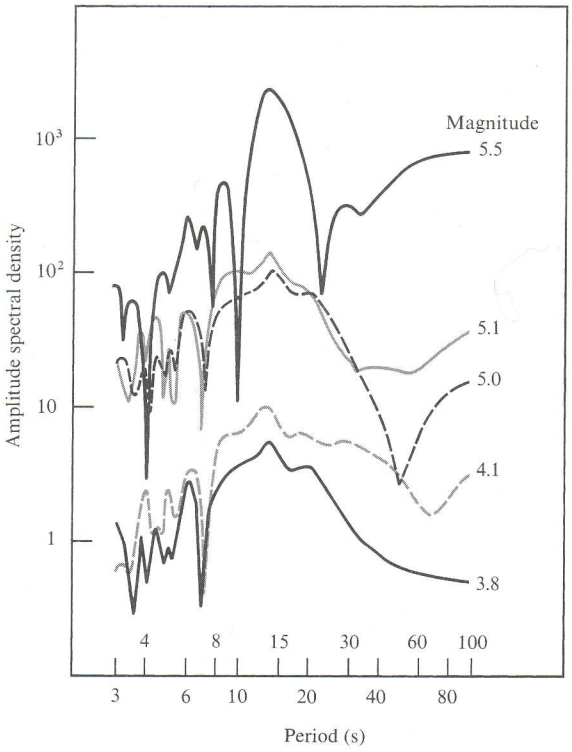

FIGURE **10.4**
Amplitude spectra of Love waves from a series of earthquakes in Parkfield, California, recorded at Berkeley, California, at a distance of 270 km. The main shock, with local magnitude 5.5 ($M_s = 6.4$), shows nodes at 22.5, 9.8, and 7.6 s. The last node is probably a path effect, because it shows up for all earthquakes, independent of magnitude. [From Filson and McEvilly, 1967.]

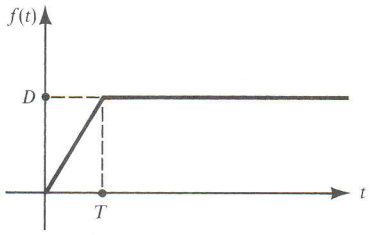

FIGURE **10.5**
Definition of rise time T.

as shown in Figure 10.5. Taking the Fourier transform of $\dot{f}(t)$ and putting it into (10.20), we obtain

$$|\Omega(\mathbf{x}, \omega)| = WLD \frac{\sin X}{X} \left| \frac{1 - e^{i\omega T}}{\omega T} \right|. \tag{10.22}$$

The effect of a finite rise time T therefore introduces additional smoothing of the waveform: for high frequencies, it attenuates the spectrum proportional to ω^{-1}. Thus the finite length of the fault over which the rupture is propagated, together with the finite time needed to complete the slip at a point on the fault, make the spectrum attenuate as ω^{-2} at high frequencies.

So far, we have introduced the following five source parameters:

(i) Fault length L.

(ii) Fault width W.

(iii) Rupture velocity v.

(iv) Permanent slip D.

(v) Rise time T.

The corresponding far-field displacement spectrum is given by (10.22). The spectrum is flat near $\omega = 0$, and the height of the flat part is proportional to DWL, or seismic moment. For frequencies higher than the reciprocals of apparent rupture time $L[1/v - (\cos \Psi)/c]$ and rise time T, the spectrum decays with frequency as ω^{-2}. If the effect of finite width is also taken into account, as done by Hirasawa and Stauder (1965), a spectral decay of ω^{-3} should be expected. Another extension of the model often used in practice is to assume that the rupture propagates from a point in the fault plane to positive and negative directions along its length. This is called bilateral faulting and the corresponding seismic spectrum can be easily obtained by appropriately superposing the results for two unilateral fault motions propagating in opposite directions.

The seismic energy, spectral density, and near-field effects of the above five-parameter model were studied in detail by Haskell (1964, 1966, 1969), and it is often called Haskell's model. For many earthquakes, reliable estimates of the product of L, W, and D have been made—and hence of the seismic moment (by assuming a value of the rigidity). The measurement of L is easier than that of W or D, because its effect can be studied using longer waves, which suffer less from complex path effects. The reliable estimation of D and T require near-field data, which are usually difficult to obtain. Types of fault slip more general than those of the Haskell model are considered in Problem 10.7, showing that the far field spectrum can still be regarded as the product of two factors, the first being associated with an equivalent point source (and having spectral decay due to the finite rise time), the second being due to the finiteness of faulting (and having spectral decay due to spatial interference).

Once the fault area and fault slip are determined, one can make a rough estimate of stress drop associated with the faulting, by referring to a crack problem of similar geometry. With some exceptions we can summarize results roughly as the statement that for most earthquakes the stress drop lies in the range from 10 to 100 bars, independent of magnitude. The slip velocity (D/T) across the fault also appears to lie in a limited range: from 10 to 100 cm/s. According to Abe's (1975) summary, the stress drop $\Delta\sigma$ and the slip velocity (D/T) appear to be related via $\Delta\sigma = \beta\rho(D/T)$, where the coefficient of proportionality, $\beta\rho$ (= shear wave speed $\times$ density), is just the impedance for plane shear waves (see Box 5.4 with angle $j = 0$).

Equations such as (10.7), (10.16), (10.22) and extensions of them such as discussed in Problem 10.7 provide the kinematic framework for interpretation of earthquake phenomena across a range of different geometries and stress drops. Thus, equation (10.7) indicates that if the slip velocity is constant, then the seismic radiation scales directly with the size of the rupture. The simplest scaling is one in which slip velocity is constant; and fault width, rise time, and final offset are all proportional to fault length. The stress drop is then constant, independent of moment, and $M_0 \propto L^3$. Abercrombie and Leary (1993) reported low-magnitude seismic data from a deep borehole in Southern California, and data from several other regions, in support of such a simple scaling law across a moment range spanning 20 orders of magnitude. Other seismologists who have drawn upon data

across a smaller but still significant magnitude range, for events all from the same region, have in some cases reported a different result, namely that stress drop appears to increase monotonically with increasing moment for events below a critical size, becoming constant for events larger than critical (e.g., Shi *et al.*, 1998). Heaton (1990) pointed out numerous earthquakes with fault length much greater than width, for which the rise time was likely to be independent of fault length, resulting in a different scaling law.

An extensive study of source parameters of major earthquakes in and near Japan was made by Kanamori and his colleagues using the Haskell model. The result, as summarized by Kanamori (1973), showed that the amount of slip and the extent of the fault area obtained by the seismic method are in good agreement with those obtained by a static method, using geodetic measurements for earthquakes caused by "brittle elastic" rebound. On the other hand, for earthquakes attributed to "visco-elastic" rebound, the slip and fault area were found to be significantly greater by the static method than by the seismic method, indicating that the seismic event does not totally represent tectonic processes associated with an earthquake. The completion of the Global Positioning Satellite system in the 1990s permits subcentimeter determination of absolute locations of points nearly anywhere on Earth, and Heki *et al.* (1997) made such a measurement of ground displacements at 16 stations in the vicinity of a magnitude 7.8 subduction zone earthquake that occurred on 1994 December 28, off the Sanriku coast of northeastern Japan. During the ensuing 12 months, the displacement of 15 of these sites grew to exceed the displacement that had occurred at the time of the earthquake at these same sites. These authors and DeMets (1997) interpreted the observations as evidence for afterslip, somewhere on the fault plane that ruptured in the main shock, rather than as an effect of viscosity in a lower layer. The motion between tectonic plates is apparently accommodated by a continuum of processes, including slow-rupture earthquakes, aseismic creep, and afterslip, as well as by more conventional earthquakes.

10.1.6 NUCLEATION, SPREADING, AND STOPPING OF RUPTURE

The unidirectional propagation of rupture in Haskell's source model is an oversimplification of faulting when we look closer at the nucleation of the rupture process. To make the model more realistic, it is desirable to allow rupture to initiate at a point (rather than simultaneously everywhere along a line segment) and then spread out radially (rather than propagate in a single direction), until it covers an arbitrary two-dimensional surface on the fault plane. Far-field waveforms from this type of source model, using a uniform rupture velocity, were first studied by Savage (1966) using equation (10.13).

As shown in Figure 10.6, we shall place the fault in the plane $x_3 = 0$ and assume that rupture propagates from the origin in all directions with uniform velocity v and stops at the perimeter of the fault plane Σ. Initially the rupture front is a circle described by $\rho = vt$, but the final fault will have a perimeter given by $\rho = \rho_b(\phi')$, where (ρ, ϕ') are cylindrical coordinates in the fault plane.

Savage (1966) assumed the displacement discontinuity was a step function in time with final value $\Delta U(\rho, \phi')$. In our notation and using Heaviside step functions, the model can be expressed as

$$\Delta u(\xi, t) = \Delta U(\rho, \phi') H(t - \rho/v)[(1 - H(\rho - \rho_b)]. \tag{10.23}$$

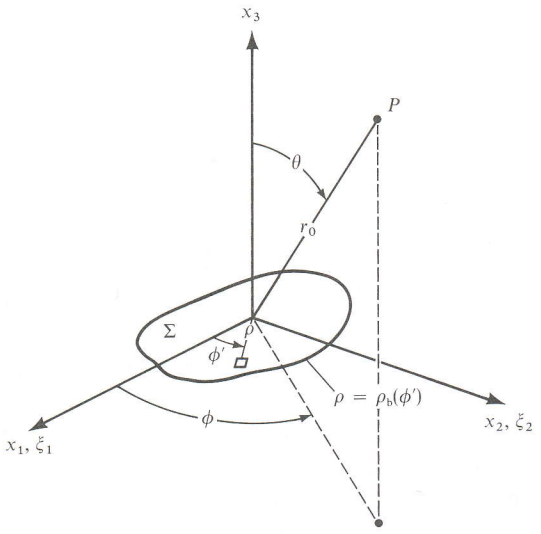

FIGURE **10.6**
The rupture starts from the origin and spreads in the x_1x_2-plane with a constant velocity v. Initially, the rupture front is a circle $\rho = vt$, but the final fault plane has a perimeter given by $\rho = \rho_b(\phi')$. P is the observation point, and an element $d\Sigma$ of the fault is shown at (ρ, ϕ').

Putting this into (10.13), we find

$$\begin{aligned}\Omega(\mathbf{x}, t) &= \iint_\Sigma \Delta\dot{u}\left(\xi, t - \frac{r_0 - (\xi \cdot \gamma)}{c}\right) d\Sigma(\xi) \\ &= \iint \delta\left(t - \frac{r_0}{c} + \frac{\rho \sin\theta \cos(\phi - \phi')}{c} - \frac{\rho}{v}\right) \Delta U(\rho, \phi') \\ &\quad \times [1 - H(\rho - \rho_b)]\rho \, d\rho \, d\phi',\end{aligned} \tag{10.24}$$

where we used the spherical coordinates shown in Figure 10.6 for expressing $(\xi \cdot \gamma)$. Since $\int f(x)\, \delta(ax - b)\, dx = f(b/a)/a$, the integration with respect to ρ gives

$$\int \delta\left(t - \frac{r_0}{c} - \frac{\rho q_c}{v}\right) \Delta U(\rho, \phi')[1 - H(\rho - \rho_b)]\rho \, d\rho$$

$$= \left(t - \frac{r_0}{c}\right) \Delta U\left(\frac{t - \dfrac{r_0}{c}}{q_c/v}, \phi'\right) \frac{v^2}{q_c^2} \qquad \text{for } 0 < \frac{t - \dfrac{r_0}{c}}{q_c/v} < \rho_b$$

$$= 0 \qquad \text{for } 0 < \frac{t - \dfrac{r_0}{c}}{q_c/v} > \rho_b,$$

where $q_c = 1 - (v/c)\sin\theta\cos(\phi - \phi')$ is assumed positive everywhere; in other words, $v < c$ and the rupture is subsonic. [If $v > c$, waves would arrive before r_0/c in the directions (θ, ϕ) for which q_c is negative, because $\Delta U[(t - r_0/c)/(q_c/v), \phi')]$ will be nonvanishing for $t < r_0/c$.]

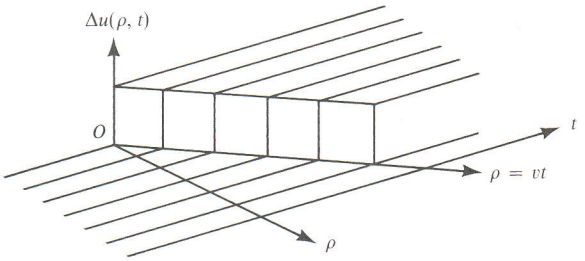

FIGURE **10.7**
Slip function for a circular fault with uniform slip.

For subsonic rupture propagation, (10.24) can be written as

$$\Omega(\mathbf{x},t) = v^2\left(t-\frac{r_0}{c}\right)H\left(t-\frac{r_0}{c}\right)\int \frac{\Delta U\left(\dfrac{t-r_0/c}{q_c/v},\phi'\right)}{q_c^2}d\phi', \qquad (10.25)$$

where the integral is taken over the range of ϕ' for which $[(t-r_0/c)/(q_c/v)v] < \rho_b$.

Suppose that the final slip ΔU is uniform except near the fault perimeter, and suppose that we look at the beginning of the far-field displacement waveform, when $t - r_0/c$ is small and the range of integration for ϕ' covers 0 to 2π. In that case, we see from (10.25) that the displacement waveform is a linear function of time (a ramp function). The linearity will hold until the rupture front reaches the perimeter of the prescribed fault surface.

Thus a subsonically spreading rupture with a uniform step-function slip generates a far-field displacement waveform $(t-r_0/c)H(t-r_0/c)$ until the stopping signal arrives from the perimeter of the fault. The corresponding particle-velocity waveform due to this type of nucleation is a step function with a discontinuity at $t = r_0/c$. The acceleration is a δ-function, reaching infinity at $t = r_0/c$. The spectral density of acceleration, velocity, and displacement are therefore constant, and proportional to ω^{-1} and ω^{-2}, respectively.

In order to see what happens when the rupture stops propagating, let us consider the case of a circular fault with uniform slip, in which $\rho_b = \rho_0$ (constant), $\Delta U(\rho,\phi') = \Delta U_0$ (constant). Then $\Delta u(\xi,t)$ is a function of ρ and t, as shown in Figure 10.7. The simplest result is obtained in the direction normal to the fault plane. For $\theta = 0$, $q_c = 1$ and equation (10.25) shows that the integral with respect to ϕ' is constant for $v(t-r_0/c) < \rho_0$ and vanishes for $v(t-r_0/c) > \rho_0$. In other words, the far-field displacement waveform $\Omega(\mathbf{x},t)$ for $\theta = 0$, which grows like a ramp function beginning at $t = r_0/c$, subsequently has a jump discontinuity at $t = r_0/c + \rho_0/v$, when $\Omega(\mathbf{x},t)$ suddenly becomes zero. This jump discontinuity gives infinite particle velocity and acceleration. The spectral density of displacement, in the high-frequency limit, will decay in proportion to ω^{-1}. A seismic signal associated with the stopping of rupture was named a "stopping phase" by Savage.

For $\theta \neq 0$, $q_c = 1 - (v/c)\sin\theta\cos(\phi-\phi')$ is a function of ϕ', taking its minimum value in the azimuth $\phi' = \phi$ to the station and its maximum in the opposite azimuth $\phi' = \phi + \pi$. Since $\Delta U(\rho,\phi')$ is constant and q_c is a smooth function, the integral in equation (10.25) is proportional to the range of ϕ' for which $[v(t-r_0/c)]/q_c < \rho_0$. As long as the locus of $\rho = [v(t-r_0/c)]/q_c$ is contained inside the circle $\rho = \rho_0$, the integration range of ϕ' is 2π.

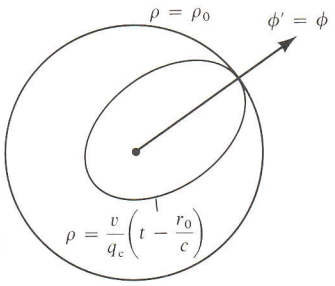

FIGURE **10.8**

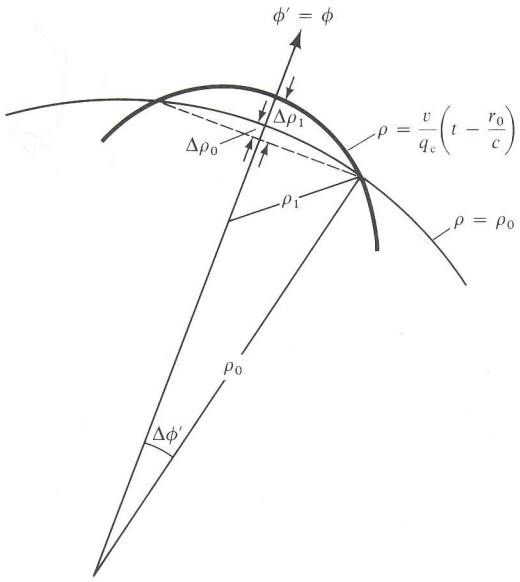

FIGURE **10.9**

Since the minimum of q_c is at $\phi' = \phi$, the locus of $\rho = [v(t - r_0/c)]/q_c$ will touch the circle $\rho = \rho_0$ first at $\phi' = \phi$, as shown in Figure 10.8. The growth $\Delta\phi'$ of the portion of ϕ' for which $[v(t - r_0/c)]/q_c > \rho_0$ can be found from the geometry shown in Figure 10.9.

Expressing ρ_1 as the radius of curvature of $\rho = [v(t - r_0/c)]/q_c$ at the point of contact, and taking into account the relation

$$\Delta\rho_0 = \rho_0 - \sqrt{\rho_0^2 - (\rho_0 \Delta\phi')^2} \sim (\rho_0/2)(\Delta\phi')^2$$

and a similar relation for $\Delta\rho_1$, we get

$$\Delta\rho = \Delta\rho_1 - \Delta\rho_0 \sim \left(\frac{\rho_0^2}{2\rho_1} - \frac{\rho_0}{2}\right)(\Delta\phi')^2.$$

Since $\Delta\rho$ is proportional to the time Δt after the two curves make contact, the integration range $\Delta\phi'$ will be proportional to $\sqrt{\Delta t}$, and the far-field displacement $\Omega(\mathbf{x}, t)$ will

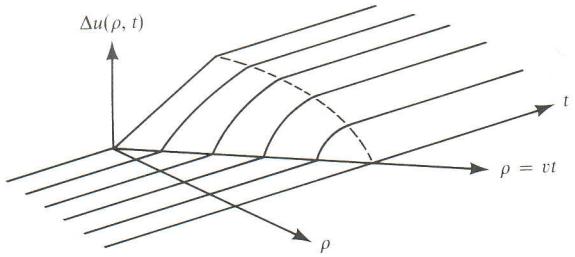

FIGURE **10.10**
Slip function for a circular fault on which the shear stress is constant.

therefore have a sudden change proportional to $\sqrt{\Delta t}$. The corresponding spectral density for displacement will have a high-frequency asymptotic limit decaying as $\omega^{-3/2}$. Both the particle velocity and acceleration will be infinite at the arrival of this stopping phase. Thus the stopping phase ($\propto \omega^{-3/2}$) dominates the nucleation phase ($\propto \omega^{-2}$) at high frequencies in this model. For the special direction $\theta = 0$ the stopping phase is even stronger ($\propto \omega^{-1}$), as would be expected since the stopping of rupture becomes apparent, in retarded time, at the same instant from all points on the perimeter of this circular fault as rupture ceases.

As can be seen from the derivation given above, the $\omega^{-3/2}$ frequency dependence (for $\theta \neq 0$) applies not only to the stopping of a circular crack front but to that of any smoothly curved crack front.

There are some unrealistic aspects about the above model as an example of shear fracture. First, the slip is not consistent with the known static solution; and second, the stopping of slip in the interior of the fault occurs everywhere instantaneously and therefore has no causal relationship with the stopping of the rupture front. The first point was partially taken into account by Savage (1966) but was more fully considered by Sato and Hirasawa (1973), who assumed the following slip function:

$$\begin{aligned} \Delta u(\rho, t) &= K\sqrt{(vt)^2 - \rho^2}\, H(t - \rho/v)[1 - H(\rho - \rho_0)] && \text{for } vt < \rho_0 \\ &= K\sqrt{\rho_0^2 - \rho^2}\, [1 - H(\rho - \rho_0)] && \text{for } vt > \rho_0, \end{aligned} \tag{10.26}$$

where

$$K = \left(\frac{24}{7\pi}\right)\left(\frac{\Delta\sigma}{\mu}\right).$$

This model is constructed by assuming that Eshelby's (1957) static solution holds at every successive instant of rupture formation for a circular crack under uniform shear stress (see Fig. 10.10). Putting equation (10.26) into equation (10.13) it is possible to carry out the integration exactly, and Sato and Hirasawa obtained the following compact result:

$$\begin{aligned} \Omega(\mathbf{x}, t) &= 2K v\rho_0^2[\pi/(1-k^2)^2]x^2 && \text{for } 0 < x < 1-k \\ &= 2K v\rho_0^2(\pi/4)[1/k - (x^2/k)(1+k)^{-2}] && \text{for } 1-k < x < 1+k, \end{aligned} \tag{10.27}$$

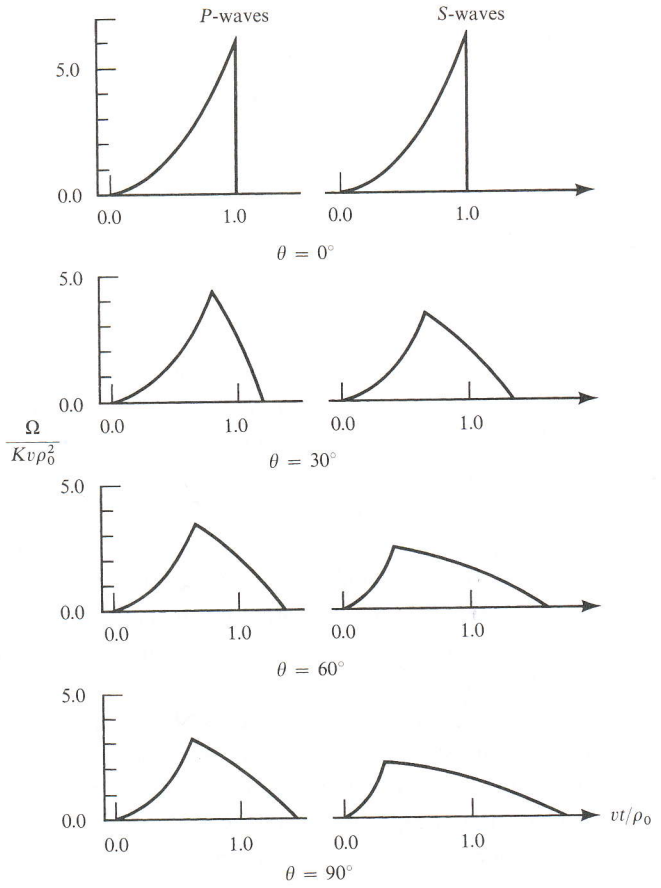

FIGURE **10.11**
Far-field wave forms according to equation (10.27); θ is defined in Figure 10.6. [From Sato and Hirasawa, 1973.]

where $k = (v/c)\sin\theta$ and $x = v(t - r_0/c)/\rho_0$. An example of $\Omega(\mathbf{x}, t)$ is shown in Figure 10.11. The initial rise of the far-field displacement is now proportional to $(t - r_0/c)^2$ instead of $(t - r_0/c)$ as in the previous case of uniform step-function slip. The spectral density corresponding to this rising part will have high-frequency asymptotic decay proportional to ω^{-3}. The spectral density for the total waveform, however, shows a high-frequency asymptotic decay of ω^{-2}, indicating once again that the stopping phase dominates the nucleation phase at high frequencies. The ω^{-2} decay is expected for this case because of an additional $\omega^{-1/2}$ due to the square root dependence of the slip function on distance from the crack tip, as compared with the uniform-slip case in which we obtained the $\omega^{-3/2}$ decay.

A defect of Sato and Hirasawa's model is that particle motions cease at the same instant, everywhere over the fault plane. Let us now look at another kinematic model of circular rupture, proposed by Molnar, Tucker, and Brune (1973). The slip-velocity function for this model is given by

$$\Delta\dot{u}(\rho, t) = \Delta V \left[H\left(t - \frac{\rho}{v} + \frac{\rho_0}{v}\right) - H\left(t + \frac{\rho}{v} - \frac{\rho_0}{v}\right) \right] H(\rho_0 - \rho), \quad (10.28)$$

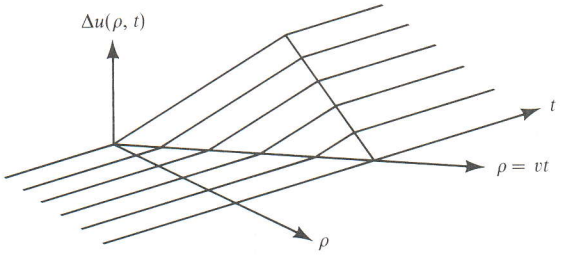

FIGURE **10.12**
Slip function for a circular fault on which a "healing front" (bringing motions to a stop) propagates inward after the fault has reached its final size.

where ρ_0 is the radius of a circular ruptured area and ΔV is the relative particle velocity (assumed to be constant over the area). The rupture nucleates at the center, grows radially in all directions at a constant velocity v to the radius ρ_0, and then contracts back to the center at the same velocity. This is a crude kinematic model of the spontaneous rupture process in which slip starts with the arrival of the rupture front and continues until information from the edges of the fault is radiated back to each point of the interior. The slip function of this model is shown in Figure 10.12.

Putting the Fourier transform of (10.28) into (10.15) and evaluating the integral, Molnar *et al.* obtained the high-frequency asymptotic decay as ω^{-2} to ω^{-3} depending on θ. The $\omega^{-5/2}$ decay is expected for a stopping phase in this case because of an additional ω^{-1} due to the linear dependence of the slip function on distance from the crack tip, as compared with the uniform-slip case in which we obtained the $\omega^{-3/2}$ decay.

As far as the initial part is concerned, this slip function is simply a time integral of the one for the uniform step-function case (equation (10.23)). Therefore, the initial rise of far-field displacement is the time-integral of linear increase. It is thus a parabolic increase, in common with the model of Sato and Hirasawa.

Dahlen (1974) extended the analysis of rupture kinematics to an elliptical crack that keeps on growing with the same shape. He used the following slip function, obtained by Burridge and Willis (1969) as an exact solution of the self-similar problem of an expanding elliptical crack:

$$\Delta u(\xi, t) = \Delta V \sqrt{t^2 - \frac{\xi_1^2}{u^2} - \frac{\xi_2^2}{v^2}}\, H\left[t - \sqrt{\frac{\xi_1^2}{u^2} + \frac{\xi_2^2}{v^2}}\right], \tag{10.29}$$

where ΔV is the relative velocity across the center of the crack, and u and v are rupture-propagation velocities in the ξ_1- and ξ_2-directions, respectively. As we shall see in Section 11.1.4, the slip function (10.29) leads to a uniform stress drop on the fracture surface, and thus is a solution of the crack problem as long as the crack continues to grow self-similarly (see Box 10.1). If $u = v$, the above equation reduces to (10.26) for the circular crack considered by Sato and Hirasawa for $t < \rho_0/v$. The initial rise of far-field displacement is again parabolic, and the corresponding high-frequency asymptotic decay is proportional to ω^{-3}. Unlike the models discussed earlier, Dahlen's model considers the rupture as being slowly brought to a halt as the crack edge propagates into regions of either increasing

BOX **10.1**
On the concept of "self-similarity"

A self-similar wave-propagation phenomenon is one for which there is no intrinsic length scale or time scale, so that the phenomenon appears the same at all scales of space and time. Commonly, there is a resulting simplicity in the space–time dependence of the propagating wave that can allow an exact solution of the displacements and stresses, for all $(\mathbf{x}, t)$.

For example, the solution to Lamb's problem (the waves set up throughout a homogeneous elastic half-space by an impulse applied to its surface) is self-similar. If distances from the source are doubled in a fixed direction from the source, the shape of the exact waveform at the second distance—the complete waveform in this case is made up from the P-wave, S-wave, and Rayleigh wave—is derived from the first waveform by doubling the time scale. But if the impulse is applied at a fixed depth rather than at the surface, this depth provides a scale length and the resulting wave solution is not self-similar.

The waves set up in an elastic whole space by the slip function given in (10.29) are self-similar, as is apparent from inspection of the solution for this problem presented in Section 11.1.4. Note that we can write this slip function in terms of a dimensionless time coordinate $t' = t/T$ and dimensionless space coordinates $\xi_i' = \xi_i/L_i$ $(i = 1 \text{ or } 2)$, for our choice of constants T, L_1, L_2. The resulting expression is

$$\Delta u(\xi, t) = \Delta V \cdot T \sqrt{t'^2 - \frac{\xi_1'^2}{u'^2} - \frac{\xi_2'^2}{v'^2}}\, H\left[t' - \sqrt{\frac{\xi_1'^2}{u'^2} + \frac{\xi_2'^2}{v'^2}}\right],$$

where $u' = (T/L_1)u$ and $v' = (T/L_2)v$ are dimensionless parameters related to rupture velocities. The ability to represent key variables in dimensionless form is another feature of self-similar solutions.

friction or decreasing tectonic stress. For such a slow stopping process he concluded that the nucleation phase would dominate the stopping phase at high frequencies.

If we neglect the contribution from the stopping phase, the high-frequency limits of the far-field spectrum can be obtained by putting the Fourier transform of (10.29) into equation (10.15). The result is given by

$$|\Omega(\mathbf{x}, \omega)| = \frac{4\pi u v\, \Delta V \omega^{-3}}{\left(1 - \frac{u^2}{c^2}\sin^2\theta\cos^2\phi - \frac{v^2}{c^2}\sin^2\theta\sin^2\phi\right)^2}, \tag{10.30}$$

where θ and ϕ are defined in Figure 11.7. Since (10.30) does not contain parameters involving the final size of the crack, this model predicts a high-frequency behavior that is independent of earthquake size. On the other hand, if the stopping phase dominates at high frequencies, the size of the earthquake will be a factor, and the high-frequency values of $|\Omega|$ for larger earthquakes will be larger than for small ones. We shall come back to this point later in the discussion of scaling laws for seismic spectra.

10.1.7 CORNER FREQUENCY AND THE HIGH-FREQUENCY ASYMPTOTE

As shown in preceding sections, the far-field displacement due to any reasonable kinematic model of an earthquake is expected to have a spectrum with a constant value at low frequencies and proportional to a negative power of frequency at high frequencies. Following Brune (1970), we shall define a corner frequency as the frequency at the intersection of the low- and high-frequency asymptotes in the spectrum. The far-field spectrum is then roughly characterized by three parameters: (i) the low-frequency level, which is proportional to seismic moment; (ii) the corner frequency; and (iii) the power of the high-frequency asymptote.

Let us find the corner frequency as a function of source parameters for some of the kinematic models discussed earlier. We shall find that a major disagreement arises among various models concerning the relative magnitude of the P-wave and S-wave corner frequencies.

Savage (1972) calculated the corner frequencies for P- and S-waves assuming bilateral faulting with rupture velocity v and final fault length L:

$$\begin{aligned} \Delta u(\xi, t) &= D_0 G(t - \xi_1/v) && 0 \le \xi_1 < L/2 \\ &= D_0 G(t + \xi_1/v) && -L/2 < \xi_1 < 0 \\ &= 0 && \text{otherwise,} \end{aligned} \tag{10.31}$$

where

$$\begin{aligned} G(t) &= 0 && t < 0 \\ &= 1 - \exp(-t/T) && 0 \le t. \end{aligned}$$

Assuming that the rise time T is equal to the travel time of the rupture front over half a fault width, i.e., $T = W/2v$, Savage obtained the corner frequency as a geometric mean of two corner frequencies associated with the finite rupture propagation and the rise time. In this case, the high-frequency asymptote is proportional to ω^{-2}. Assuming further that $v = 0.9\beta$, the corner frequency averaged over all directions is obtained as

$$2\pi \langle f_P \rangle = \sqrt{2.9} \cdot \alpha / \sqrt{LW} \tag{10.32}$$

for P-waves and

$$2\pi \langle f_S \rangle = \sqrt{14.8} \cdot \beta / \sqrt{LW} \tag{10.33}$$

for S-waves. For a normal Poisson's ratio, the above formula shows for this model of fault slip that the P-wave corner frequency is lower than the S-wave corner frequency.

However, Furuya (1969) observed that the predominant period of S-waves is 1.3 to 1.5 times greater than that of P-waves for a given magnitude, implying that $\langle f_P \rangle$ is higher than $\langle f_S \rangle$, and he pointed out that the simple propagating fault model cannot explain such observations. The majority of subsequent observational studies of corner frequency support $\langle f_P \rangle > \langle f_S \rangle$.

The circular-crack model of Sato and Hirasawa also gives an asymptote like ω^{-2}, as discussed in the preceding section, but predicts higher corner frequency for P-waves than

TABLE **10.1**
Table of C_P and C_S values appearing in (10.34) and (10.35)

v/β	C_P	C_S
0.5	1.11	1.53
0.6	1.25	1.70
0.7	1.32	1.72
0.8	1.43	1.76
0.9	1.53	1.85

for S-waves, in accordance with observations. Their corner frequencies averaged over all directions are

$$2\pi \langle f_P \rangle = C_P \alpha / R \tag{10.34}$$

for P-waves and

$$2\pi \langle f_S \rangle = C_S \beta / R \tag{10.35}$$

for S-waves, where R is the radius of the crack and C_P and C_S are functions of rupture velocity, as shown in Table 10.1.

In this case, $\langle f_P \rangle$ is higher than $\langle f_S \rangle$, and their ratio varies from 1.26 to 1.43 as v/β increases from 0.5 to 0.9. Sato and Hirasawa attribute the inadequacy of fault models of the type considered by Haskell to the restrictive form of $\Delta u(\xi, t)$ given in (10.17) or (10.31), where the time-dependence is assumed to be common to all the points on the fault. This assumption may be approximately valid for a long thin fault in which the slip function is determined by the width alone, but it is poor for an equidimensional fault in which the rupture nucleates at a point and spreads out to all directions on the fault plane. Both their model and the model of Molnar *et al.* (described in Section 10.1.6), which also predicts $\langle f_P \rangle > \langle f_S \rangle$, are free from this restriction. As we shall discuss in Section 11.1.5, some of the important features of the solution to a dynamic problem of finite circular crack formation are contained in the models of Sato and Hirasawa, and of Molnar *et al.*

On the other hand, formula (10.30) for a self-similar elliptical crack predicts lower corner-frequency for P-waves than for S-waves. The formula is based on the assumption that the nucleation phase dominates the stopping phase at high frequencies. The high-frequency asymptote given in (10.30) is determined by the rupture velocities and the particle velocity. Since the rupture velocities are given as material constants and the particle velocity is determined by rupture velocities and the initial stress, the asymptote in this case is determined independent of the size of the final ruptured area: at a given travel distance the far-field seismic waves would have the same absolute spectrum for frequencies higher than

the corner frequency, independent of earthquake magnitude, if formula (10.30) is correct. This result appears to contradict observations on the scale effect on seismic spectra, as discussed below.

An observed seismic spectrum is a function of source, path, and receiver. The simplest way of eliminating the path and receiver effects is to compare seismograms obtained by the same seismograph at the same station from two earthquakes with the same epicenter. Berckhemer (1962) was able to collect six such earthquake pairs recorded at the Stuttgart station for the period 1931–1951, and found a strong frequency dependence of amplitude ratios between the pair. These data were interpreted by Aki (1967) using two kinematic models: the ω-square and ω-cube models. The ω-cube model is a special case of the earthquake model suggested by Haskell (1966) and has the exact property described in the previous paragraph (a high-frequency spectrum that is independent of earthquake size). The far-field displacement spectrum for the ω-cube model is expressed as

$$S(\omega) = \frac{S(0)}{[1 + (\omega/\omega_0)^2]^{3/2}}, \tag{10.36}$$

where $S(0)$ is proportional to seismic moment. The value of ω_0 is effectively the corner frequency, though in practice it may differ somewhat from the definition given previously in terms of the intersection between high- and low-frequency asymptotes (see Shi *et al.*, 1998). As discussed in Section 10.1.5, if we assume similarity between large and small earthquakes the seismic moment will be proportional to L^3. The corner frequency will be proportional to L^{-1}, so we have

$$S(0) = \text{const.} \times \omega_0^{-3}. \tag{10.37}$$

Once the above constant is fixed, a family of spectral curves is determined that will describe the scaling law of seismic spectra. Neighboring curves shown in Figure 10.13 are separated by a constant factor at frequency 0.05 Hz, so that the curves are designated by a uniform scale of M_s defined by Gutenberg and Richter (Appendix 2) using the amplitude of surface waves at a period of 20 s. If the M_s of one curve is fixed, then M_s is determined for the rest. One can then find the amplitude ratio between two earthquakes of any magnitude as a function of frequency. By trial and error, Aki (1967) found the family of spectral curves, shown in Figure 10.13, which best fit Berckhemer's observed amplitude ratio. These spectral curves share the same high-frequency asymptote in the absolute sense, independent of earthquake magnitude. This feature is expected when the nucleation is responsible for the high-frequency asymptote as in Dahlen's model: the effect may be observed for the initial portion of the seismogram in which the effect of stopping has not appeared. In fact, the body-wave magnitude m_b (Appendix 2), defined by the amplitude of short-period (about 1 s) P-waves in the first 5 s, reaches a maximum value at around $m_b = 6$ and does *not* increase with earthquake size (Geller, 1976). This is in agreement with the spectral curves of Figure 10.13, which show that the spectral density at frequencies of 1 Hz and higher is the same for all M_s greater than 5.5.

BOX 10.2

Allowance for finite faulting in calculating far-field body waves within depth-dependent structures

In all our chapters on wave propagation in heterogeneous media, we have used very simple sources, usually a point source. But to explain seismic data it is necessary to merge the theories of wave propagation with the source theory we are developing in this chapter and the next. Provided we can make the Fraunhofer approximation, based on (10.12), all that is needed for purposes of computing the radiation from finite faulting is to know the slip function $[\mathbf{u}(\xi, \tau)]$ over the fault Σ, and the Green function $\mathbf{G}(\mathbf{x}, t; \xi, \tau)$.

Thus, in the far-field it is often adequate to make the approximation

$$\mathbf{G}(\mathbf{x}, t; \xi, \tau) \sim \mathbf{G}\left(\mathbf{x}, t; \mathbf{0}, \tau - \frac{\xi \cdot \gamma}{c}\right) \tag{1}$$

for that part of the wave field at $\mathbf{x}$ associated with waves having velocity $c(\xi)$ in the source region. Here γ is a unit vector at the origin of coordinates (taken on Σ); and γ is in the direction of waves departing from Σ.

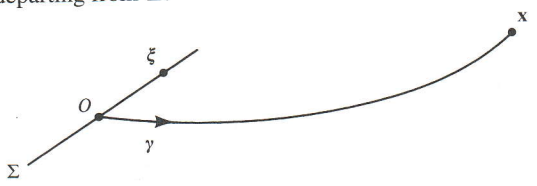

The approximation (1) above is equivalent to approximation (10.11), which was used in deriving (10.13). When the Green function is integrated over Σ, we need only make an allowance for the far-field phase correction (i.e., the travel-time difference) between ξ and O. This is appropriate for far-field body waves and surface waves in depth-varying and laterally-varying media.

For example, in Chapter 9 we obtained integrals over ray parameter p that gave far-field body-wave pulse shapes in depth-varying media. Point sources were used, and often the source was characterized by $M_0(\omega)$, together with some strike, dip, and rake (see, e.g., (9.96) and (9.102)). To generalize these results in order to allow for finite faulting, it is clear that one must replace

$$M_0(\omega) \qquad \text{by} \qquad \iint_\Sigma \mu \, \Delta u(\xi, \omega) \exp\left[-\frac{i\omega(\xi \cdot \gamma)}{c(\xi)}\right] d\Sigma \tag{2}$$

(assuming slip in the same direction everywhere over Σ).

Note that γ itself is dependent on ray parameter, so that the expression (2) should appear within the integration over p which characterized much of our numerical work in Chapter 9. However, for many practical purposes it is adequate to evaluate (2) at one representative value of γ for each $\mathbf{x}$.

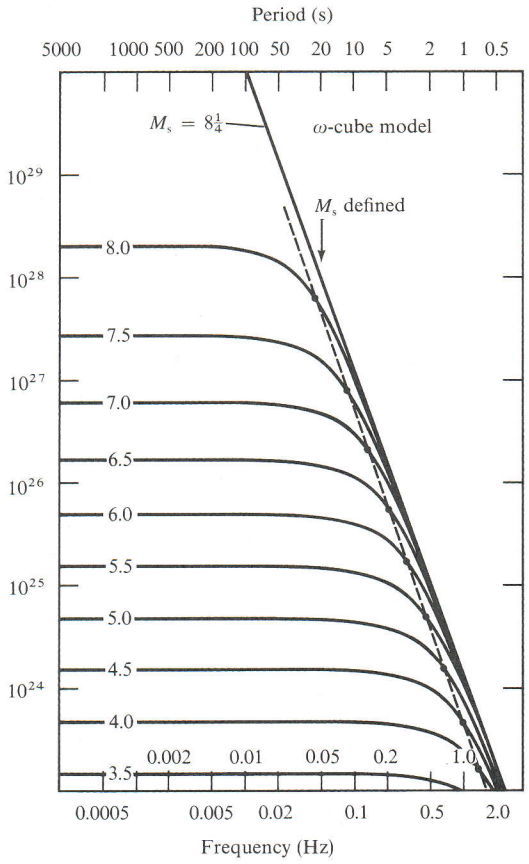

FIGURE **10.13**
Spectra of far-field body-wave displacement observed at a fixed distance from earthquakes with different M_s. The vertical coordinate shows the corresponding seismic moment. All curves share the common shape of equation (10.36), and similarity between large and small earthquakes is assumed. The broken line is the locus of the corner frequency ω_0. [From Aki, 1967; copyright by the American Geophysical Union.]

The curves in Figure 10.13, however, do not seem to apply to the total seismogram. The duration of seismic signal is longer for larger earthquakes, so if the spectral density is independent of magnitude, it follows that larger earthquakes should show smaller amplitudes for frequencies higher than 1 Hz. This clearly contradicts the observation on peak accelerations for $6 < M < 8$, as shown later in Figure 12.13. Peak accelerations observed at short distances are at frequencies higher than 1 Hz, and they are greater for larger earthquakes at a given distance.

Fortunately, Aki's ω-square model gives more satisfactory results. This model has the far-field spectrum given by

$$S(\omega) = \frac{S(0)}{\left[1 + (\omega/\omega_0)^2\right]}. \tag{10.38}$$

The corresponding family of spectral curves fitting the Berckhemer data is shown in Figure 10.14. In this case, the spectral amplitude increases with magnitude M_s for all frequencies, in agreement with observation.

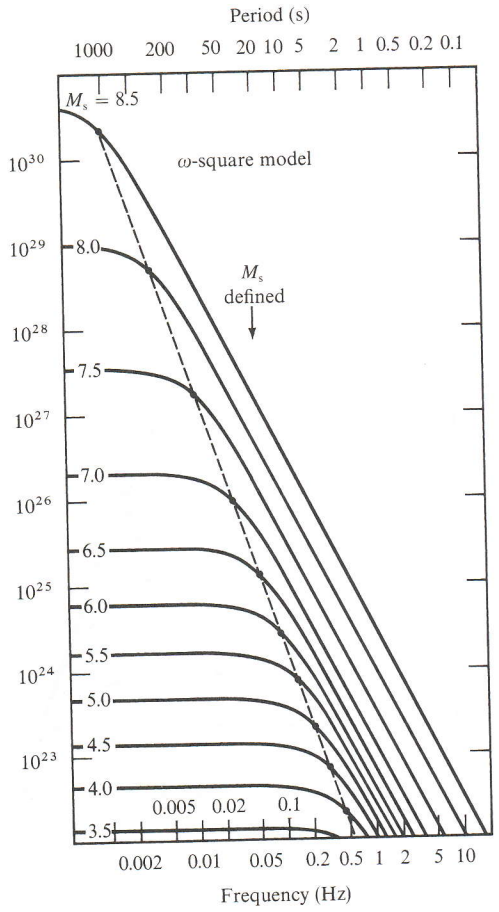

FIGURE **10.14**
Same as Figure 10.13 except that the spectra share the common shape of equation (10.38). The broken line is the locus of ω_0. [From Aki, 1967; copyright by the American Geophysical Union.]

That the high-frequency spectrum for the ω-square model should increase with magnitude without ceiling was expected because the ω^{-2} asymptote indicates the dominance of a stopping phase at high frequencies, and the number of stopping points (or the length of stopping loop) increases with the ruptured area. There was a ceiling for the ω-cube model, because the nucleation point is a single point for any earthquake.

10.2 Kinematics of an Earthquake as Seen at Near Field

In the preceding section, we studied seismic waves observed in the far field, for which a simple relation (10.13) exists between the waveform and the fault slip function. There are, however, two major drawbacks to the study of seismic sources from far-field observation. First, as shown by (10.15), the far-field waves carry information about the source function only for that part of the space-time spectrum for which $|\omega/k| > c$, where ω is the frequency, k is the wavenumber component in the fault plane, and c is the wave-propagation velocity. A complete determination of the slip function requires observation near the seismic source. Second, the waves recorded in the far field had to travel a long distance from the source.

During the propagation, waves will suffer from attenuation, scattering, spreading, focusing, multipath interference, and other complex path effects. One way of minimizing the path effects is to make observations at a short distance from the seismic source, again leaning upon the near-field data for more complete study of the source mechanism.

Ideally, we wish to measure the slip function $\Delta u(\xi, t)$ at various points ξ directly on the fault plane. Since such a measurement is almost impossible in practice, we must find out how the seismic motion close to but at some distance from the fault is related to the slip on the fault. This relation is complicated because the seismograms at short distances are composed of far-field and near-field terms of P- and S-waves coming from each element of the fault, as discussed in Section 4.2. These different terms cannot be isolated on the records, and therefore the total seismogram must be computed for comparison with observations. Such a computation is useful also for predicting seismic effects at the site of an engineering structure, due to a nearby earthquake fault on which the kinematic motions have been prescribed.

10.2.1 SYNTHESIS OF NEAR-FIELD SEISMOGRAMS FOR A FINITE DISLOCATION

The near-field seismic motion for a finite dislocation source buried in a homogeneous, isotropic, unbounded medium can be calculated by integrating the solution obtained in Section 4.2 for seismic displacement due to an infinitesimal fault $d\Sigma$ across which the slip is given as $[\mathbf{u}(\xi, t)]$. The solution for an arbitrary slip function over a finite fault surface $\Sigma(\xi)$ can be obtained using equation (4.30), or equations (10.1) and (10.2), as

$$
\begin{aligned}
u_i(\mathbf{x}, t) = \iint_{\Sigma} \mu \Bigg[& \left(\frac{30\gamma_i n_p \gamma_p \gamma_q \nu_q - 6\nu_i n_p \gamma_p - 6n_i \gamma_q \nu_q}{4\pi\rho r^4} \right) \\
& \times \left(F\left(t - \frac{r}{\alpha}\right) - F\left(t - \frac{r}{\beta}\right) + \frac{r}{\alpha}\dot{F}\left(t - \frac{r}{\alpha}\right) - \frac{r}{\beta}\dot{F}\left(t - \frac{r}{\beta}\right) \right) \\
& + \left(\frac{12\gamma_i n_p \gamma_p \gamma_q \nu_q - 2\nu_i n_p \gamma_p - 2n_i \gamma_q \nu_q}{4\pi\rho\alpha^2 r^2} \right) \Delta u\left(\xi, t - \frac{r}{\alpha}\right) \\
& - \left(\frac{12\gamma_i n_p \gamma_p \gamma_q \nu_q - 3\nu_i n_p \gamma_p - 3n_i \gamma_q \nu_q}{4\pi\rho\beta^2 r^2} \right) \Delta u\left(\xi, t - \frac{r}{\beta}\right) \\
& + \frac{2\gamma_i n_p \gamma_p \gamma_q \nu_q}{4\pi\rho\alpha^3 r} \Delta \dot{u}\left(\xi, t - \frac{r}{\alpha}\right) \\
& - \left(\frac{2\gamma_i n_p \gamma_p \gamma_q \nu_q - \nu_i n_p \gamma_p - n_i \gamma_q \nu_q}{4\pi\rho\beta^3 r} \right) \Delta \dot{u}\left(\xi, t - \frac{r}{\beta}\right) \Bigg] d\Sigma(\xi),
\end{aligned}
\tag{10.39}
$$

where $F(t) = \int_0^t dt' \int_0^{t'} \Delta u(\xi, t'')\, dt''$, $\mathbf{n}\, \Delta u(\xi, t) = [\mathbf{u}]$, ν is the fault normal, $r = |\mathbf{x} - \xi|$, and $\gamma = (\mathbf{x} - \xi)/r$. Each of the terms under the surface integral has a simple form identifiable as waves propagating either as P or S, attenuating as a certain negative power

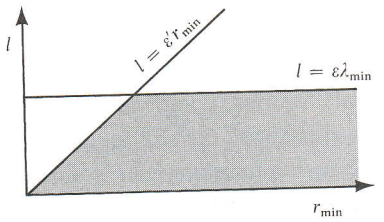

FIGURE **10.15**

of distance from the source. The waveform of each term can be easily calculated for a given slip function $\Delta u(\xi, t)$. It is difficult, however, to make a general statement on the total displacement because, at short distances, those terms arrive almost simultaneously, often canceling each other because they are of comparable size, so that the behavior of the sum of all the terms is quite unpredictable from separate consideration of individual terms. This is especially true for motion close to the fault, because each term tends to infinity as $r \to 0$, although physically we expect the sum of all the terms to be finite (see Problem 4.1).

Early work on evaluating the near field of finite faulting was based mostly on the direct numerical integration of (10.39) with respect to ξ. For a numerical integration of (10.39), we replace the integral by a summation over grid points, assuming that the integrand varies smoothly in the grid interval. Each term of the integrand in (10.39) contains two distinct factors: one is a negative power of $r = |\mathbf{x} - \xi|$, and the other is a function directly derivable from $\Delta u(\xi, t - r/c)$, where c is the wave velocity. Subsequent work on the evaluation of (10.39) has entailed making an efficient choice of grid size, and associated approximations, as we next discuss.

For r^{-n} to be smooth over $(r_0, r_0 + l)$, nl/r_0 must be negligible as compared to 1. Therefore, the grid interval l must be taken to be much smaller than $r_{\min}/n$, where $r_{\min}$ is the minimum distance from the observation point $\mathbf{x}$ to the fault plane $\Sigma(\xi)$.

The smoothness of the other factor is determined by the slip-time function. Since $\Delta u(\xi, t - r/c)$ contains $t - r/c$ in place of the time variable of the slip function, it varies rapidly as a function of ξ over a distance l if the slip function varies rapidly over a time interval l/c. For this factor to be smooth over the grid interval l, l/c must be much smaller than the minimum period $T_{\min}$ contained in the slip function. For example, if the slip function is characterized by the rise time T, then l must be much smaller than cT. The choice of l is restricted by the above two conditions to the shaded region of Figure 10.15, where $\lambda_{\min}$ is the wavelength corresponding to $T_{\min}$, and ε and ε' are small fractions.

For a relatively large $r_{\min}$, we can relax the above restriction on l to some degree by the same approximate method used for the far-field calculation in Section 10.1.3. If l^2 is much less than $r_{\min} \cdot \lambda_{\min}$, then from (10.11) applied to each grid interval we can put

$$r = r_0 - (\boldsymbol{\gamma} \cdot \xi),$$

where $\boldsymbol{\gamma}$ is the unit vector directed from a grid point to the observation point. Then we can get a compact result for the integral over each grid interval, assuming that the factor r^{-n} is constant. For example, if we set the time dependence of $\Delta u(\xi, t)$ as $\exp(-i\omega t)$, the integral

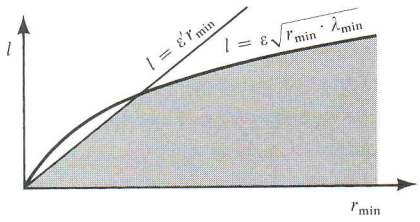

FIGURE **10.16**

over the grid interval will have a factor $(x^{-1} \sin x)e^{ix}$, where $x = \omega l/2(1/v - c^{-1} \cos \Psi)$, as defined in Section 10.1.5. We can then sum these integrated terms over all the grid points. The time-domain solution for a given slip function can be synthesized for the solutions for various ω. The appropriate choice of l for this method will be in the shaded region of Figure 10.16, which allows a coarser grid (larger l) for much of the spatial region than is the case in Figure 10.15.

Both methods have been used in interpreting the records of strong-motion (or low-magnification) seismographs located at short distances from earthquakes, and several interesting results have been obtained from comparison with observations. For example, for a Haskell-type moving dislocation (10.21) with slip motion parallel to the direction of rupture propagation, it was predicted that the displacement near the fault in the direction perpendicular to the fault plane should have an impulsive form with amplitude being a significant fraction of the amount of slip and with width being nearly equal to the rise time. Such an impulsive displacement with the expected sense of motion was actually observed by a strong-motion seismograph located only 80 meters from the San Andreas fault during the Parkfield earthquake of 1966 June 28. Figure 10.17 shows the perpendicular component of the acceleration, velocity, and displacement. A slightly different displacement record was published by Housner and Trifunac (1967), who used an integration technique different from the one used to obtain Figure 10.17. Figure 10.18 shows the theoretical displacement seismogram synthesized for a unilaterally propagating fault. The rise time and slip for the models that fit the observation are about 0.4–0.9 s and 60–100 cm, respectively. Although these estimates of source parameters had to be revised by later work of Bouchon (1979), who also included the effect of a low-velocity sedimentary layer, the successful comparison between the theoretical and experimental results encouraged seismologists to pursue further the synthesis of strong motion near an earthquake fault.

Numerical integration methods were also used by Anderson and Richards (1975) in a comparative study of the near-field motion for Haskell's model with that calculated for several different kinematic models of faulting. They found that it is often difficult in practice to determine the slip function from kinematic modeling, even when several records of ground motion are available within one fault length from the source region.

In order to simulate ground motion in Southern California associated with a hypothetical large earthquake on the San Andreas fault, Olsen *et al.* (1995) modeled a strike slip source kinematically with $\Delta\dot{u}$ taken to have a gaussian shape, moving along strike with a rupture velocity equal to 85% of the local S-wave speed. They used finite differencing to solve for the wave propagation in an inhomogeneous crustal structure described by a

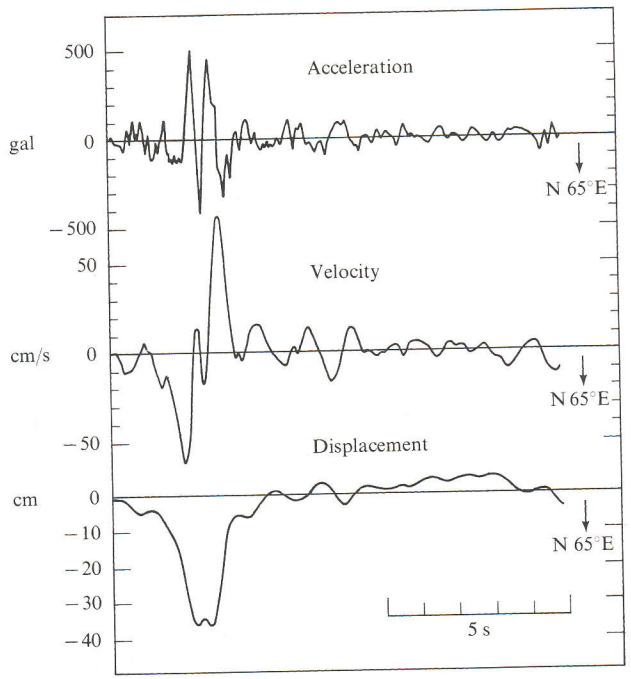

FIGURE **10.17**
Acceleration, velocity, and displacement observed at 80 meters from the San Andreas fault in the direction perpendicular to the fault trace during the 1966 Parkfield earthquake. [From Aki, 1968; copyright by the American Geophysical Union.]

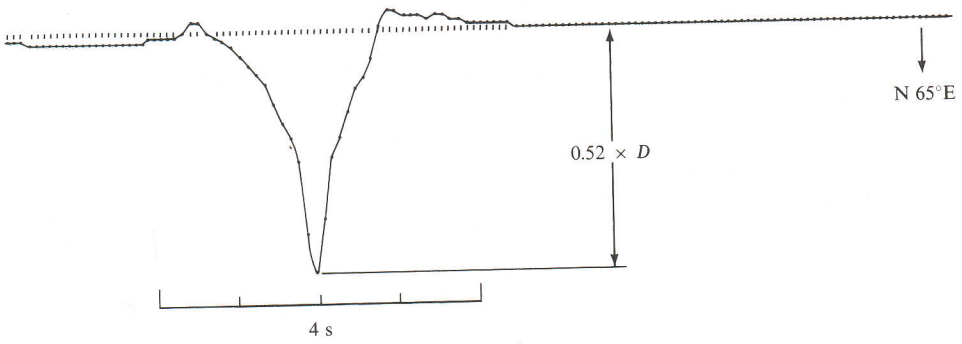

FIGURE **10.18**
Synthetic displacement corresponding to the observation shown in Figure 10.17 for a right-lateral strike slip fault propagating with rupture velocity 2.2 km/s. [From Aki, 1968; copyright by the American Geophysical Union.]

three-dimensional grid with 576 points along strike, 352 points perpendicular to strike, and 116 points in the depth direction. Body waves and surface waves were included, and the finite difference solution was integrated for points on the gridded fault surface, and over the source duration. The simulation of ground motion over about 20,000 km^2 of crustal surface for a duration of two minutes took about 24 hours on a machine with 512 processors. They found that the ground motion is amplified by a factor of about 2.5 at some locations, over that for a uniform layered model with overall similar properties.

Such numerical-integration methods described above can be very useful and are entirely appropriate when crustal structure is well known, but they are time-consuming and do not always give good physical insight. Thus one cannot generalize the behavior of seismic motion. It must be calculated for each specific case. This limitation is especially severe for high-frequency waves.

To overcome this limitation, compact, exact analytic solutions have been sought for simplified source models. For example, Boatwright and Boore (1975) and Sato (1975) showed that analytic solutions may be obtained for Haskell's model in the case when the fault width W becomes zero. The other extreme model is the case when W becomes infinity, reducing the problem to two dimensions. This reduction may be justified for frequencies higher than a certain critical frequency f_c determined by the minimum distance r_{min} to the fault from the station and by the width W of the fault plane: if the station is close to the fault plane, the seismic motion will be independent of W for frequencies higher than f_c. For two-dimensional problems, we can find compact and exact solutions more easily, as shown in Sections 10.2.3 and 10.2.4. The result will be useful for understanding the high-frequency motions—especially the nature of ground accelerations near the fault, which could not effectively be studied by the numerical method described above.

10.2.2 HIGH-FREQUENCY MOTIONS NEAR A PROPAGATING FAULT

To gain physical insight into the near field of a propagating fault, we shall consider greatly simplified models and obtain analytical solutions for the resulting motions. Let us put the fault in the zx-plane, with its rupture front parallel to the z-axis and propagating in the x-direction, as shown in Figure 10.19. For a nearby observation point on the xy-plane, the effect of the width of the fault on high-frequency motions may be neglected and we can use the solution for two-dimensional problems in which the fault width is set equal to infinity. This simplifies the analysis greatly, because every quantity becomes independent of z.

We shall consider two basic types of propagating faults: anti-plane and in-plane. For the anti-plane type with rupture propagation in the x-direction, the slip is in the z-direction as shown in Figure 10.19, and the resulting displacement has a component only in the z-direction. In crystal-dislocation theory, this is called a *screw dislocation*, in which the slip direction (Burger's vector) is parallel to the dislocation line. If the fault plane is horizontal, the resulting motions are composed solely of SH-waves. For the in-plane type, the slip is in

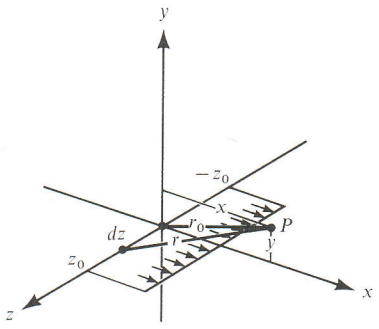

FIGURE **10.19**

the x-direction, and the resulting displacement has x- and y-components, associated with both P- and SV-waves. In crystal-dislocation theory, this is called an *edge dislocation*, in which the slip direction is perpendicular to the dislocation line. When the edge-dislocation line moves in the direction parallel to the slip, the movement is called *gliding*.

10.2.3 ANTI-PLANE PROBLEMS

As the simplest anti-plane problem, we shall consider the case in which phenomena appear to be stationary if looked at in coordinates

$$x' = x - vt, \qquad y' = y, \qquad t' = t,$$

which move with a constant velocity v. Such a case is possible for a semi-infinite fault plane propagating with velocity v from the time $-\infty$. The condition on the discontinuity in the displacement $w(x, y, t)$ across the fault plane is given by

$$w(x, +0, t) - w(x, -0, t) = \Delta w H(-x'), \tag{10.40}$$

where $H(x)$ is the unit step function. The stress is assumed to be continuous, so that

$$\mu \frac{\partial w}{\partial y}(x, +0, t) = \mu \frac{\partial w}{\partial y}(x, -0, t). \tag{10.41}$$

The equation of motion for an isotropic homogeneous body reduces to a wave equation for w:

$$\frac{1}{\beta^2} \frac{\partial^2 w}{\partial t^2} = \frac{\partial^2 w}{\partial x^2} + \frac{\partial^2 w}{\partial y^2}. \tag{10.42}$$

Using the new coordinates, and applying the stationarity condition $\partial/\partial t' = 0$, i.e.,

$$\frac{\partial}{\partial t} = \frac{\partial}{\partial t'} - v\frac{\partial}{\partial x'} = -v\frac{\partial}{\partial x'}, \qquad \frac{\partial}{\partial x} = \frac{\partial}{\partial x'}, \qquad \frac{\partial}{\partial y} = \frac{\partial}{\partial y'},$$

equation (10.42) can be rewritten as

$$\left(1 - \frac{v^2}{\beta^2}\right) \frac{\partial^2 w}{\partial x'^2} + \frac{\partial^2 w}{\partial y'^2} = 0. \tag{10.43}$$

For $v = 0$, this reduces to the Laplace equation and its solution for boundary conditions (10.40) and (10.41) is based on properties of $\log(x' + iy')$ and is well known. We use the fact that the imaginary part of $\log(x' + iy')$ satisfies the Laplace equation, so the solution of (10.43) when $v = 0$, that is discontinuous (but with continuous derivative) across $y = 0$ is

$$w(x', y') = A \tan^{-1} \frac{y'}{x'} \qquad \text{for some constant } A.$$

The function $\tan^{-1}$ here is taken to lie in the range $(-\pi, \pi)$. Since $w(x', y')$ is a solution of the Laplace equation, $w(x'/\sqrt{1 - v^2/\beta^2}, y')$ will be a solution of (10.43). Here we have assumed subsonic rupture propagation, $v < \beta$. Our solution of (10.42) is therefore given by

$$w(x, y, t) = \frac{\Delta w}{2\pi} \tan^{-1} \frac{y\sqrt{1 - v^2/\beta^2}}{x - vt} \tag{10.44}$$

where the constant A has been assigned the value $\Delta w/(2\pi)$. This satisfies the boundary conditions (10.40), requiring the continuity of w everywhere except at $y = 0$, $x < vt$, because (10.44) does correctly give

$$\begin{aligned} w(x, y, t) &= 0 && \text{at } y = 0, x > vt \\ &= \frac{\Delta w}{2} && \text{at } y = +0, x < vt \\ &= -\frac{\Delta w}{2} && \text{at } y = -0, x < vt. \end{aligned}$$

Since the stress components are

$$\begin{aligned} \tau_{xz} &= -\frac{\mu\, \Delta w}{2\pi} \frac{\sqrt{1 - v^2/\beta^2} \cdot y}{(x - vt)^2 + (1 - v^2/\beta^2)y^2}, \\ \tau_{yz} &= \frac{\mu\, \Delta w}{2\pi} \frac{\sqrt{1 - v^2/\beta^2}\,(x - vt)}{(x - vt)^2 + (1 - v^2/\beta^2)y^2}, \end{aligned} \tag{10.45}$$

τ_{xz} vanishes at $y = 0$, and the condition (10.41) is satisfied at $y = 0$, where

$$\tau_{yz} = \mu \frac{\partial w}{\partial y} = \mu \frac{\Delta w}{2\pi} \frac{\sqrt{1 - v^2/\beta^2}}{x - vt}. \tag{10.46}$$

The stress τ_{yz} on the plane $y = 0$ is an odd function of $x - vt$, and becomes $-\infty$ behind the tip and $+\infty$ ahead of the tip. Note that τ_{yz} vanishes when the rupture velocity is β. Equation (10.44) was obtained by Frank (1949), Liebfried and Dietze (1949), and Eshelby (1949).

The particle velocity is obtained from (10.44) as

$$\frac{\partial w}{\partial t} = \frac{\Delta w}{2\pi} \frac{yv\sqrt{1 - v^2/\beta^2}}{(x - vt)^2 + y^2(1 - v^2/\beta^2)}. \tag{10.47}$$

The peak velocity occurs at $x = vt$, and the peak value is $(\Delta w/2\pi) \cdot [v/(y\sqrt{1 - v^2/\beta^2})]$. The peak value tends to infinity as the rupture velocity approaches β for this semi-infinite crack. It decays as the inverse of distance from the fault.

The acceleration can be obtained from (10.47) as

$$\frac{\partial^2 w}{\partial t^2} = \frac{\Delta w}{2\pi} \cdot \frac{2y(x - vt)v^2\sqrt{1 - v^2/\beta^2}}{[(x - vt)^2 + y^2(1 - v^2/\beta^2)]^2}.$$

The peak acceleration occurs at $x - vt = (y/\sqrt{3})\sqrt{1 - v^2/\beta^2}$, and is

$$\frac{\Delta w}{2\pi} \frac{9}{8\sqrt{3}} \frac{v^2}{y^2(1 - v^2/\beta^2)}.$$

The peak acceleration also tends to infinity as the rupture velocity approaches β. It decays as the inverse square of distance from the fault.

The nature of motions in the near field of a propagating dislocation may be better interpreted from their spectrum. The Fourier transform of $\partial w/\partial t$ at $x = 0$ can be obtained by residue evaluation at poles $t = \pm iy\sqrt{1 - v^2/\beta^2}/v$, and is equal to

$$\frac{\Delta w}{2} \exp\left(-|y| \cdot |\omega| \cdot \frac{\sqrt{1 - v^2/\beta^2}}{v}\right).$$

This shows an exponential decay with both y and ω, indicating that they are composed of inhomogeneous plane waves trapped near the fault plane. Thus, for a subsonic rupture propagation with uniform velocity that starts at time $-\infty$ and continues to time $+\infty$, the near-field motion decays quickly with the distance y from the fault plane; the peak velocity decays as y^{-1}, and the peak acceleration as y^{-2}. The spectrum decays exponentially with increasing frequency, as expected for inhomogeneous plane waves.

Next let us introduce simple models of starting and stopping in the fault propagation, and see what will happen in the near field. To study the effect of starting, we shall replace (10.40) with the following boundary condition:

$$w(x, +0, t) - w(x, -0, t) = \Delta w \cdot H\left(t - \frac{x}{v}\right) H(x), \tag{10.48}$$

which corresponds to a step-function slip starting from $x = 0$ at $t = 0$ and propagating in the $+x$-direction with velocity v, as shown in Figure 10.19. Since the motion is not stationary in the moving coordinates, equation (10.43) no longer applies. Expressing the Laplace transform of $w(x, y, t)$ as

$$w(x, y, s) = \int_0^\infty w(x, y, t) e^{-st}\, dt,$$

we rewrite the equation of motion (10.42) as

$$\frac{s^2}{\beta^2} w = \frac{\partial^2 w}{\partial x^2} + \frac{\partial^2 w}{\partial y^2}. \tag{10.49}$$

Taking the Laplace transform of the boundary condition (10.48), we have

$$w(x, +0, s) - w(x, -0, s) = \frac{\Delta w \cdot e^{-sx/v}}{s} H(x). \tag{10.50}$$

Since

$$e^{-sx/v} H(x) = \frac{1}{2\pi} \int_{-\infty}^{\infty} \frac{e^{ikx}}{i(k - is/v)} dk,$$

which can be obtained easily by residue evaluation of the pole at $k = is/v$, the boundary condition (10.50) can be rewritten as

$$w(x, +0, s) = -w(x, -0, s) = \frac{\Delta w}{4\pi s} \int_{-\infty}^{\infty} \frac{e^{ikx}}{i(k - is/v)} dk, \tag{10.51}$$

where we have used the antisymmetry with respect to y: $w(x, -y, t) = -w(x, y, t)$.

To meet the above boundary condition, we assume the solution of (10.49) has the form

$$w(x, y, s) = \int_{-\infty}^{\infty} Q(k) e^{ikx - \nu y}\, dk,$$

where $\nu^2 = k^2 + s^2/\beta^2$. $Q(k)$ is determined by putting $y = \pm 0$ and comparing with (10.51). The result is

$$\begin{aligned} w(x, y, s) &= \frac{\Delta w}{4\pi s} \int_{-\infty}^{\infty} \frac{e^{ikx - \nu y}}{i(k - is/v)} dk, \qquad y > 0 \\ &= -\frac{\Delta w}{4\pi s} \int_{-\infty}^{\infty} \frac{e^{ikx + \nu y}}{i(k - is/v)} dk, \qquad y < 0. \end{aligned} \tag{10.52}$$

The stress $\mu(\partial w/\partial y)$ is continuous at $y = 0$.

Equation (10.52) has a familiar form to which the Cagniard method is applicable (Mitra, 1966; Boore and Zoback, 1974). Transforming the variable k to τ by the relation

$$-s\tau = ikx - \sqrt{k^2 + s^2/\beta^2}\, y,$$

(10.52) is reduced to

$$\begin{aligned} w(x, y, s) = &-\frac{\Delta w}{2\pi} \int_0^{\infty} \mathrm{Re} \frac{\sqrt{\tau^2 - r^2/\beta^2} \cos\theta - i\tau \sin\theta}{\sqrt{\tau^2 - r^2/\beta^2} \sin\theta + i(\tau \cos\theta - r/v)} \\ &\times \frac{H(\tau - r/\beta)}{\sqrt{\tau^2 - r^2/\beta^2}} \frac{e^{-s\tau}}{s} d\tau, \end{aligned}$$

where $x = r\cos\theta$ and $y = r\sin\theta$. Since the above equation now has the form of the Laplace transform for $sw(x, y, s)$, the corresponding time-domain solution $\partial w(x, y, t)/\partial t$ can be identified as

$$\begin{aligned} \frac{\partial w(x, y, t)}{\partial t} = &\frac{\Delta w}{2\pi} \frac{(t^2 - r^2/\beta^2) \sin\theta \cos\theta - t \sin\theta (t \cos\theta - r/v)}{(t^2 - r^2/\beta^2) \sin^2\theta + (t\cos\theta - r/v)^2} \\ &\times \frac{H(t - r/\beta)}{\sqrt{t^2 - r^2/\beta^2}}. \end{aligned} \tag{10.53}$$

This equation reduces to (10.47) for the dislocation propagating from $t = -\infty$ if we make θ small and $x \to vt$. In other words, the near-field motion at the time of arrival of a rupture front is approximately explained by the simple solution given in equation (10.47).

The new solution, however, contains an additional sharp waveform originating from the starting points at $t = 0$ and propagating with the velocity of shear waves. The particle velocity is unbounded at $t = r/\beta$, where it has a square-root singularity. Near $t = r/\beta$, (10.53) becomes approximately

$$\frac{\partial w}{\partial t} = \frac{\Delta w}{2\pi} \frac{\sin\theta}{(\beta/v - \cos\theta)} \frac{1}{\sqrt{2r/\beta}} \frac{H(t - r/\beta)}{\sqrt{t - r/\beta}}. \tag{10.54}$$

This wave attenuates with distance as $1/\sqrt{r}$, representing a cylindrical wave that originates at the starting point of the fault propagation, and shows a radiation pattern given by $\sin\theta/(\beta/v - \cos\theta)$. For example, the x-direction along which the fault is propagating is a node. The spectrum of particle velocity $\partial w/\partial t$ given in (10.54) has a high-frequency asymptote of $1/\sqrt{\omega}$.

The acceleration associated with this "starting phase" has a singularity of the form $(t - r/\beta)^{-3/2} H(t - r/\beta)$ near the shear-wave arrival, and the corresponding spectrum has a high-frequency asymptote of $\sqrt{\omega}$.

If the slip function is a ramp function (equation (10.21)) instead of a step function, the peak particle velocity will be finite, but the peak acceleration will have a square-root singularity at $t = r/\beta$.

The effect of stopping can be studied by superposition of another moving dislocation starting at, say, $x = L$ at $t = L/v$, propagating with the same velocity v, but with opposite sign of slip. This will annihilate the fault ahead of $x = L$, and gives the solution for a finite fault that started at $x = 0$ and stopped at $x = L$. We then obtain another singularity propagating from the stopping point as cylindrical waves. The nature of this "stopping" phase is nothing but the "starting" phase of the superposed second fault. The equivalence here of stopping and starting is due to the unidirectional nature of fault propagation. If the rupture starts from a point and grows over an expanding area, the two effects will be quite different, as discussed in Section 10.1.6 for the far field.

Note that all the two-dimensional anti-plane faults in this section generate SH-waves alone.

10.2.4 IN-PLANE PROBLEMS

The simplest in-plane problem (Fig. 10.19) is the semi-infinite fault plane moving with a constant velocity v from time $-\infty$, and it generates both P-waves and SV-waves. We shall consider the case of a step-function slip, in which the boundary condition is written as

$$u(x, +0, t) - u(x, -0, t) = \Delta u \cdot H(-x'), \tag{10.55}$$

where $x' = x - vt$. The y-component of displacement, $v(x, y, t)$, and the traction on the fault plane, are continuous across $y = 0$.

The displacement components that satisfy the equation of motion in the in-plane problem can be written in terms of two scalar potentials as

$$u(x, y, t) = \frac{\partial \phi}{\partial x} - \frac{\partial \psi}{\partial y}, \qquad v(x, y, t) = \frac{\partial \phi}{\partial y} + \frac{\partial \psi}{\partial x} \tag{10.56}$$

(see Section 5.1 for development of two scalar potentials for two-dimensional $P-SV$ problems). The potentials ϕ and ψ satisfy the following wave equations:

$$\frac{1}{\alpha^2}\frac{\partial^2\phi}{\partial t^2}=\frac{\partial^2\phi}{\partial x^2}+\frac{\partial^2\phi}{\partial y^2}, \qquad \frac{1}{\beta^2}\frac{\partial^2\psi}{\partial t^2}=\frac{\partial^2\psi}{\partial x^2}+\frac{\partial^2\psi}{\partial y^2},$$

where $\alpha=\sqrt{(\lambda+2\mu)/\rho}$ and $\beta=\sqrt{\mu/\rho}$ are P and S velocities, respectively. Using the moving-coordinate system (compare with the development of (10.43)), the wave equations can be rewritten as

$$\left(1-\frac{v^2}{\alpha^2}\right)\frac{\partial^2\phi}{\partial x'^2}+\frac{\partial^2\phi}{\partial y^2}=0, \qquad \left(1-\frac{v^2}{\beta^2}\right)\frac{\partial^2\psi}{\partial x'^2}+\frac{\partial^2\psi}{\partial y^2}=0.$$

We consider here only subsonic motion, i.e., $v<\alpha$ and $v<\beta$.

The above equations have solutions of the form

$$\exp(ikx'\pm\sqrt{1-v^2/\alpha^2}\,ky) \text{ for } \phi, \qquad \text{and} \qquad \exp(ikx'\pm\sqrt{1-v^2/\beta^2}\,ky) \text{ for } \psi.$$

Since there are no sources of waves at infinity, we require that ϕ and ψ propagate away from $y=0$. For $y>0$, then, we introduce coefficients $\acute{\phi}$ and $\acute{\psi}$ in terms of which

$$\phi=\acute{\phi}\exp(ikx'-\sqrt{1-v^2/\alpha^2}\,|k|y), \qquad \psi=\acute{\psi}\exp(ikx'-\sqrt{1-v^2/\beta^2}\,|k|y), \quad (10.57)$$

and similarly for $y<0$,

$$\phi=\grave{\phi}\exp(ikx'+\sqrt{1-v^2/\alpha^2}\,|k|y), \qquad \psi=\grave{\psi}\exp(ikx'+\sqrt{1-v^2/\beta^2}\,|k|y),$$

As usual, we express the displacement u, v in terms of $\acute{\phi}$, $\acute{\psi}$, $\grave{\phi}$, and $\grave{\psi}$ using (10.56). The stress components τ_{xy} and τ_{yy} are related to displacement by

$$\tau_{yy}=\lambda\left(\frac{\partial u}{\partial x}+\frac{\partial v}{\partial y}\right)+2\mu\frac{\partial v}{\partial y}, \qquad \tau_{xy}=\mu\left(\frac{\partial u}{\partial y}+\frac{\partial v}{\partial x}\right). \quad (10.58)$$

The condition of discontinuity for u (see (10.55)) and the condition of continuity for v, τ_{xy}, τ_{yy} give four equations to determine four unknowns $\acute{\phi}$, $\acute{\psi}$, $\grave{\phi}$, and $\grave{\psi}$. The continuity of v and τ_{xy} imposes the following constraint on $(\acute{\phi}+\grave{\phi})$ and $(\acute{\psi}-\grave{\psi})$:

$$-\sqrt{1-v^2/\alpha^2}(\acute{\phi}+\grave{\phi})+i(\acute{\psi}-\grave{\psi})=0,$$

$$2i\sqrt{1-v^2/\alpha^2}(\acute{\phi}+\grave{\phi})+(2-v^2/\beta^2)(\acute{\psi}-\grave{\psi})=0.$$

The determinant of coefficients here is

$$\begin{vmatrix} -\sqrt{1-v^2/\alpha^2} & i \\ 2ik\sqrt{1-v^2/\alpha^2} & 2-v^2/\beta^2 \end{vmatrix}=-\sqrt{1-v^2/\alpha^2}\cdot v^2/\beta^2,$$

and it does not vanish as long as $v \neq \alpha$, so we must have

$$\acute{\phi} + \grave{\phi} = 0, \qquad \acute{\psi} - \grave{\psi} = 0.$$

From this, we find that $u(x, y, t)$ and $\tau_{yy}(x, y, t)$ are odd functions of y, and $v(x, y, t)$ and $\tau_{xy}(x, y, t)$ are even functions of y. Since the function τ_{yy} must be continuous at $y = 0$, it must vanish at $y = 0$:

$$\tau_{yy} = 0 \qquad \text{at } y = 0. \tag{10.59}$$

Since u is an odd function, the discontinuity condition (10.55) can be rewritten as

$$u(x, +0, t) = -u(x, -0, t) = \frac{\Delta u}{2} H(-x') = -\frac{\Delta u}{4\pi} \int_{-\infty+i\varepsilon}^{\infty+i\varepsilon} \frac{e^{ikx'}}{ik} dk, \tag{10.60}$$

where ε is a small positive number.

From the conditions (10.59) and (10.60), we can determine $\acute{\phi}$ and $\acute{\psi}$ for each k and express u and v as an integral of (10.57) with respect to k. The result for $y > 0$ is

$$\begin{aligned} u(x, y, t) = &-\frac{\Delta u}{2\pi} \int_{-\infty+i\varepsilon}^{+\infty+i\varepsilon} \left[\frac{\beta^2}{v^2} \exp\left(-\sqrt{1 - v^2/\alpha^2}\, |k| y\right) \right. \\ &\left. - \frac{(\beta^2 - v^2/2)}{v^2} \exp\left(-\sqrt{1 - v^2/\beta^2}\, |k| y\right) \right] e^{ikx'} \cdot \frac{dk}{ik}, \\ v(x, y, t) = &-\frac{\Delta u}{2\pi} \int_{-\infty+i\varepsilon}^{+\infty+i\varepsilon} \left[\frac{\beta^2}{v^2} \sqrt{1 - v^2/\alpha^2} \exp\left(-\sqrt{1 - v^2/\alpha^2}\, |k| y\right) \right. \\ &\left. - \frac{(\beta^2 - v^2/2)}{v^2 \sqrt{1 - v^2/\beta^2}} \exp\left(-\sqrt{1 - v^2/\beta^2}\, |k| y\right) \right] i \operatorname{sign}(\operatorname{Re} k) \cdot e^{ikx'} \frac{dk}{ik}, \end{aligned}$$

where sign(Re k) means the sign of the real part of k. Putting $y = 0^+$, we get the desired value $u(x, 0, t) = (\Delta u/2) \cdot H(-x')$. The integrand decays exponentially with k and y, showing that they are superpositions of inhomogeneous plane waves, as in the anti-plane case. We expect, therefore, that they are trapped near the fault plane and attenuate quickly with distance from the fault. Both components show a similar amplitude spectrum, but there is a $\pi/2$ phase shift between the two components indicated by the factor i in the integrand for $v(x, y, t)$. If $u(x, y, t)$ is antisymmetric with respect to $x' = 0$, then $v(x, y, t)$ will be symmetric. We shall see shortly that for the step-function slip, the transverse component displacement $v(x, y, t)$ shows an impulsive form with a logarithmic singularity at $x' = 0$.

To avoid the singularity at $k = 0$, we shall first evaluate the particle velocities $\partial u/\partial t$ and $\partial v/\partial t$. Since $\partial/\partial t$ introduces a factor $-ikv$ in the integrand that removes the singularity,

we can put $\varepsilon = 0$. Then the integrals will be either of the form

$$\begin{aligned}
&\int_{-\infty}^{\infty} \exp\left(ikx' - \sqrt{1 - v^2/\alpha^2}\,|k|y\right) dk \\
&\quad = \int_0^{\infty} \exp\left(ikx' - \sqrt{1 - v^2/\alpha^2}\,ky\right) dk + \int_{-\infty}^{0} \exp\left(ikx' + \sqrt{1 - v^2/\alpha^2}\,ky\right) dk \\
&\quad = \frac{2\sqrt{1 - v^2/\alpha^2}\,y}{x'^2 + (1 - v^2/\alpha^2)y^2}
\end{aligned} \tag{10.61}$$

or of the form

$$\begin{aligned}
&\int_{-\infty}^{\infty} i\ \mathrm{sign}(k) \exp\left(ikx' - \sqrt{1 - v^2/\alpha^2}\,|k|y\right) dk \\
&= \int_0^{\infty} i \exp\left(ikx' - \sqrt{1 - v^2/\alpha^2}\,ky\right) dk - \int_{-\infty}^{0} i\ \exp\left(ikx' + \sqrt{1 - v^2/\alpha^2}\,ky\right) dk \\
&= \frac{-2x'}{x'^2 + (1 - v^2/\alpha^2)y^2}.
\end{aligned} \tag{10.62}$$

We can also recognize that (10.61) is the derivative of $-2\tan^{-1}\left(\sqrt{1 - v^2/\alpha^2}\,y/x'\right)$ and that (10.62) is the derivative of $\log[x'^2 + (1 - v^2/\alpha^2)y^2]$ with respect to x'. Using these relations, we obtain the particle velocity for $y > 0$ as

$$\begin{aligned}
\frac{\partial u(x, y, t)}{\partial t} = -v\frac{\partial u(x, y, t)}{\partial x'} &= \frac{v\ \Delta u}{\pi}\left[\frac{\beta^2}{v^2}\frac{\sqrt{1 - v^2/\alpha^2}\cdot y}{x'^2 + (1 - v^2/\alpha^2)y^2}\right. \\
&\quad \left. - \frac{(\beta^2 - v^2/2)}{v^2}\frac{\sqrt{1 - v^2/\beta^2}\cdot y}{x'^2 + (1 - v^2/\beta^2)y^2}\right], \\
\frac{\partial v(x, y, t)}{\partial t} = -v\frac{\partial v(x, y, t)}{\partial x'} &= -\frac{v\ \Delta u}{\pi}\left[\frac{\beta^2}{v^2}\sqrt{1 - v^2/\alpha^2}\frac{x'}{x'^2 + (1 - v^2/\alpha^2)y^2}\right. \\
&\quad \left. - \frac{(\beta^2 - v^2/2)}{v^2\sqrt{1 - v^2/\beta^2}}\frac{x'}{x'^2 + (1 - v^2/\beta^2)y^2}\right]
\end{aligned} \tag{10.63}$$

and the displacement for $y > 0$ as

$$\begin{aligned}
u(x, y, t) &= \frac{\Delta u}{\pi}\left[\frac{\beta^2}{v^2}\tan^{-1}\frac{\sqrt{1 - v^2/\alpha^2}\cdot y}{x'} - \frac{(\beta^2 - v^2/2)}{v^2}\tan^{-1}\frac{\sqrt{1 - v^2/\beta^2}\cdot y}{x'}\right], \\
v(x, y, t) &= \frac{\Delta u}{2\pi}\left\{\frac{\beta^2}{v^2}\sqrt{1 - v^2/\alpha^2}\log\left(x'^2 + (1 - v^2/\alpha^2)y^2\right)\right. \\
&\quad \left. - \frac{(\beta^2 - v^2/2)}{v^2\sqrt{1 - v^2/\beta^2}}\log\left(x'^2 + (1 - v^2/\beta^2)y^2\right)\right\}.
\end{aligned} \tag{10.64}$$

The above formula was first obtained by Eshelby (1949), and turns out to be valid for $y < 0$ as well as for $y > 0$. Values of $\tan^{-1}$ lie in the range $(-\pi, \pi)$, so that there is a step discontinuity in u of amount Δu across $y = 0$ for $x' < 0$. This is the fault plane, and (10.64) correctly reproduces the discontinuity (10.60). The transverse component $v(x, y, t)$ shows an impulsive symmetric form with a logarithmic singularity $\log |x'|$ at $x' = 0$ or $x = vt$. This result qualitatively agrees with the result of the numerical solution discussed in Section 10.2.1 in relation to the record of the Parkfield earthquake.

The stress components may be obtained from (10.63) and (10.57) as

$$\tau_{xx} = \frac{2\mu\ \Delta u \beta^2}{\pi v^2}\left[\frac{(v^2/\alpha^2 - v^2/2\beta^2)\sqrt{1 - v^2/\alpha^2}\ y}{x'^2 + (1 - v^2/\alpha^2)y^2} + \frac{(1 - v^2/2\beta^2)\sqrt{1 - v^2/\beta^2}\ y}{x'^2 + (1 - v^2/\beta^2)y^2}\right],$$

$$\tau_{yy} = \frac{2\mu\ \Delta u \beta^2}{\pi v^2}\left[\frac{(1 - v^2/2\beta^2)\sqrt{1 - v^2/\alpha^2}\ y}{x'^2 + (1 - v^2/\alpha^2)y^2} - \frac{(1 - v^2/2\beta^2)\sqrt{1 - v^2/\beta^2}\ y}{x'^2 + (1 - v^2/\beta^2)y^2}\right],$$

$$\tau_{xy} = \frac{2\mu\ \Delta u \beta^2}{\pi v^2}\left[\frac{\sqrt{1 - v^2/\alpha^2}\ x'}{x'^2 + (1 - v^2/\alpha^2)y^2} - \frac{(1 - v^2/\beta^2)^2 x'}{\sqrt{1 - v^2/\beta^2}\,[x'^2 + (1 - v^2/\beta^2)y^2]}\right].$$

As imposed by the boundary condition (10.59), $\tau_{yy} = 0$ on the fault plane $y = 0$, and τ_{xy} is continuous across $y = 0$, where

$$\tau_{xy} = \frac{2\mu\ \Delta u \beta^2}{\pi v^2 x'}\left[\sqrt{1 - v^2/\alpha^2} - (1 - v^2/2\beta^2)^2/\sqrt{1 - v^2/\beta^2}\right]. \tag{10.65}$$

Thus, τ_{xy} has an $(x')^{-1}$ singularity at the crack tip, reaching $-\infty$ behind the tip and $+\infty$ ahead of the tip. Comparing the bracket [ ] of (10.65) with the expression given in equation (5.56) for determining the phase velocity of Rayleigh waves in a homogeneous half-space, we see that the in-plane shear stress across the fault plane vanishes when the crack tip propagates with the Rayleigh wave velocity.

For the particle velocity, the spectral contents and attenuation with distance are quite similar to those obtained earlier for the anti-plane problem. For example, the peak velocity decays inversely in proportion to the distance from the fault for both components. On the fault, the particle velocity is a δ-function for the parallel component and proportional to $(x - vt)^{-1}$ for the transverse component. Both functions have the same constant spectral density, but they differ by $\pi/2$ in phase for all frequencies. Off the fault, the high-frequency asymptote has an exponential decay, as expected for inhomogeneous plane waves.

Let us now consider the effect of a sudden start to the in-plane faulting, by solving a problem similar to the one studied in the anti-plane case (equation (10.48)). The faulting starts at $x = 0$ and propagates in the x-direction with velocity v. The boundary conditions are

$$u(x, +0, t) - u(x, -0, t) = \Delta u \cdot H(t - x/v)H(x), \tag{10.66}$$

with continuity for v, τ_{xy}, and τ_{yy} as before. Again u and τ_{yy} are odd functions of y, and v and τ_{xy} are even functions. It then follows that τ_{yy} must vanish at $y = 0$, as in the case of the fault propagated from $t = -\infty$ (see Problem 14.2, for a general result in three dimensions).

Working with potentials (10.56) and the Laplace transform, e.g., $\phi(x, y, s) = \int \phi(x, y, t)e^{-st}\, dt$, the equation of motion is satisfied if the potentials satisfy the following wave equations:

$$\frac{\partial^2\phi}{\partial x^2} + \frac{\partial^2\phi}{\partial y^2} = \frac{s^2}{\alpha^2}\phi, \qquad \frac{\partial^2\psi}{\partial x^2} + \frac{\partial^2\psi}{\partial y^2} = \frac{s^2}{\beta^2}\psi.$$

The solutions of these equations are of the forms $e^{ikx\pm\gamma y}$ and $e^{ikx\pm\nu y}$, where

$$\gamma^2 = k^2 + s^2/\alpha^2, \qquad \text{and} \qquad \nu^2 = k^2 + s^2/\beta^2.$$

The boundary condition for $u(x, +0, s)$ can be obtained by taking the Laplace transform of (10.66):

$$u(x, +0, s) = -u(x, -0, s) = \frac{\Delta u}{2}\frac{e^{-sx/v}}{s}H(x) = \frac{\Delta u}{4\pi s}\int_{-\infty}^{\infty}\frac{e^{ikx}\, dk}{i(k - is/v)}. \tag{10.67}$$

This condition and the vanishing τ_{yy} at $y = 0$ determine the solution for $y > 0$ as

$$u(x, y, s) = -\frac{\Delta u}{2\pi}\int_{-\infty}^{\infty}\left(\frac{\beta^2k^2}{s^2}e^{-\gamma y} - \frac{2\beta^2k^2 + s^2}{2s^2}e^{-\nu y}\right)\frac{e^{ikx}\, dk}{i(k - is/v)}$$

$$v(x, y, s) = -\frac{\Delta u}{2\pi}\int_{-\infty}^{\infty}\left[\frac{\beta^2}{s^2}ik\gamma e^{-\gamma y} - \frac{(2\beta^2k^2 + s^2)}{2\nu s^2}ike^{-\nu y}\right]\frac{e^{ikx}\, dk}{i(k - is/v)}.$$

To each term of the above integral, we can apply Cagniard's method. By transforming the variable k to either

$$\tau = \frac{1}{s}(-ikx + \gamma y) \qquad \text{or} \qquad \tau = \frac{1}{s}(-ikx + \nu y)$$

and identifying the resulting integral as a Laplace transform, we obtain

$$\frac{\partial u(x, y, t)}{\partial t} = \frac{\beta^2\,\Delta u}{\pi}\left\{\text{Im}\left[\frac{p_1^2\left(t\sin\theta + i\cos\theta\sqrt{t^2 - r^2/\alpha^2}\right)}{i/v - p_1}\right]\frac{H(t - r/\alpha)}{r\sqrt{t^2 - r^2/\alpha^2}}\right.$$

$$\left. -\text{Im}\left[\frac{(p_2^2 + 1/2\beta^2)\left(t\sin\theta + i\cos\theta\sqrt{t^2 - r^2/\beta^2}\right)}{i/v - p_2}\right]\frac{H(t - r/\beta)}{r\sqrt{t^2 - r^2/\beta^2}}\right\} \tag{10.68}$$

$$\frac{\partial v(x, y, t)}{\partial t} = \frac{\beta^2\,\Delta u}{\pi}\left\{\text{Re}\left[\frac{(p_1^2 + 1/\alpha^2)\,p_1}{i/v - p_1}\right]\frac{H(t - r/\alpha)}{\sqrt{t^2 - r^2/\alpha^2}}\right.$$

$$\left. -\text{Re}\left[\frac{(p_2^2 + 1/2\beta^2)\,p_2}{i/v - p_2}\right]\frac{H(t - r/\beta)}{\sqrt{t^2 - r^2/\beta^2}}\right\},$$

where $(x, y) = r(\cos\theta, \sin\theta)$, and

$$p_1 = \frac{1}{r}\sqrt{t^2 - \frac{r^2}{\alpha^2}}\ \sin\theta + i\frac{t}{r}\cos\theta, \qquad p_2 = \frac{1}{r}\sqrt{t^2 - \frac{r^2}{\beta^2}}\ \sin\theta + i\frac{t}{r}\cos\theta.$$

The above formulas were obtained by Ang and Williams (1959) and were used by Boore and Zoback (1974) in the interpretation of accelerograms recorded at Pacoima Dam during the San Fernando earthquake of 1971 February 9.

For points that are distant from where the faulting originates, the motion near the fault should look like the one obtained earlier in equations (10.63). Actually, if we make both y/r $(= \sin\theta)$ and $r - vt$ small, equations (10.68) reduce to (10.63). That is, the near-field motion at the time of arrival of the rupture front is approximately explained by the simple forms given in (10.63).

Equation (10.68) contains additional arrivals propagating as P- and S-waves from the starting point of rupture. Making $t - r/\alpha$ small, we find P-waves of the form

$$\begin{matrix}\frac{\partial u}{\partial t}\\ \frac{\partial v}{\partial t}\end{matrix} = \begin{matrix}\cos\theta\\ \sin\theta\end{matrix} \times \frac{\Delta u}{\pi}\frac{\beta^2}{\alpha^2}\frac{\sin 2\theta}{2(\alpha/v - \cos\theta)}\frac{H(t - r/\alpha)}{\sqrt{t - r/\alpha}\sqrt{2r/\alpha}}, \tag{10.69}$$

and making $t - r/\beta$ small, we find S-waves of the form

$$\begin{matrix}\frac{\partial u}{\partial t}\\ \frac{\partial v}{\partial t}\end{matrix} = \begin{matrix}-\sin\theta\\ \cos\theta\end{matrix} \times \frac{\Delta u}{\pi}\frac{\cos 2\theta}{2(\beta/v - \cos\theta)}\frac{H(t - r/\beta)}{\sqrt{t - r/\beta}\sqrt{2r/\beta}}. \tag{10.70}$$

As shown schematically in Figure 10.20, the radiation patterns of these waves have a double-couple symmetry modified by the factor $(\alpha/v - \cos\theta)^{-1}$ for P and $(\beta/v - \cos\theta)^{-1}$ for S. They are cylindrical waves, attenuating as $1/\sqrt{r}$. As in the case of the anti-plane solution, the particle velocity has a square-root singularity at the onset. The accelerations associated with these "starting phases" are also unbounded at the onset, where they have 3/2 power singularities. If the slip function is a ramp function, the peak particle velocity will be finite, but the peak acceleration will have a square-root singularity at the onset.

As discussed in the preceding section, the effect from stopping of the fault propagation can be obtained by superposing another moving dislocation. The stopping phases are similar to the starting phases in the case of unidirectional fault propagation.

For the Haskell model with a uniform slip function over a rectangular fault, Madariaga (1978) obtained an exact analytic solution for motions at any point in an unbounded, elastic, homogeneous medium. The solution consists of (i) cylindrical waves from the suddenly appearing initial dislocation line of length W and from the sudden arrest of rupture, and (ii) spherical waves radiated from the corners of the rectangular fault. The cylindrical waves dominate in the regions of a slab normal to the dislocation line containing the fault plane, and have the same characteristics as the cylindrical waves from the moving dislocation line given in equations (10.54), (10.69), and (10.70).

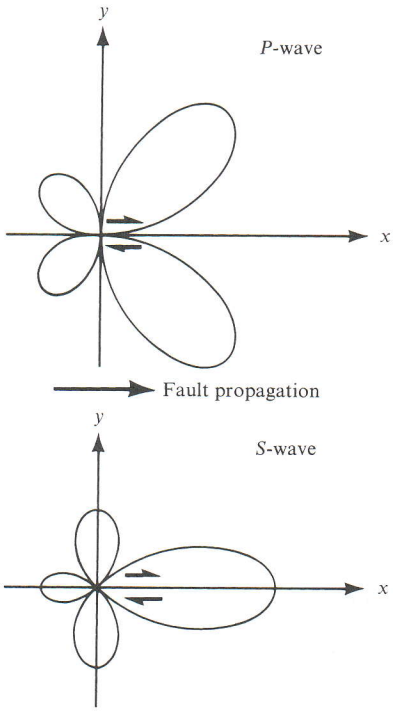

FIGURE **10.20**
Radiation patterns for the body waves radiating from the point of nucleation of a propagating in-plane shear fault. Compare with the usual double-couple radiation patterns (Figs. 4.5a and 4.6b).

Suggestions for Further Reading

Aki, K. Earthquake mechanism. *Tectonophysics*, **13**, 423–446, 1972.

Boatwright, J. The seismic radiation from composite models of faulting. *Bulletin of the Seismological Society of America*, **78**, 489–508, 1988.

Brune, J. N. Seismic source dynamics. *Reviews of Geophysics, Supplement*, **29**, 688–699, 1991.

Haskell, N. Total energy and energy spectral density of elastic wave radiation from propagating faults. *Bulletin of the Seismological Society of America*, **54**, 1811–1842, 1964; **56**, 125–140, 1966.

Heaton, T. H. Evidence for and implications of self-healing pulses of slip in earthquake rupture. *Physics of the Earth and Planetary Interiors*, **64**, 1–20, 1990.

Honda, H. Earthquake mechanism and seismic waves. *Journal of Physics of the Earth*, **10**, 1–98, 1962.

Jeffreys, H. On the mechanics of faulting. *Geological Magazine*, **79**, 291–295, 1942.

Kanamori, H. Great earthquakes at island arcs and the lithosphere. *Tectonophysics*, **12**, 187–198, 1971.

Kanamori, H. Mechanics of earthquakes. *Annual Reviews of Earth and Planetary Sciences*, **22**, 207–237, 1994.

Kanamori, H., and D. L. Anderson. Theoretical basis of some empirical relations in seismology. *Bulletin of the Seismological Society of America*, **65**, 1073–1095, 1975.

Mansinha, L., D. E. Smylie, and A. E. Beck, eds. *Earthquake Displacement Fields and the Rotation of the Earth*. New York: Springer-Verlag, 1970.

Olsen, K. B., and R. J. Archuleta. Three-dimensional simulation of earthquakes on the Los Angeles fault system. *Bulletin of the Seismological Society of America*, **86**, 575–596, 1996.

Savage, J. C. Corner frequency and fault dimensions. *Journal of Geophysical Research*, **77**, 3788–3795, 1972.

Scholz, C. H. *The Mechanics of Earthquakes and Faulting*. Cambridge University Press, 1990.

Sato, T. Seismic radiation from circular cracks growing at variable rupture velocity. *Bulletin of the Seismological Society of America*, **84**, 1199–1215, 1994.

Stevens, J. L., and S. M. Day. The physical basis of m_b: M_s and variable frequency magnitude methods for earthquake/explosion discrimination. *Journal of Geophysical Research*, **90**, 3009–3020, 1985.

Trifunac, M. D. A three-dimensional dislocation model for the San Fernando, California, earthquake of February 9, 1971. *Bulletin of the Seismological Society of America*, **64**, 149–172, 1974.

Weertman, J. Dislocations in uniform motion on slip or climb planes having periodic force laws. In *Mathematical Theory of Dislocations*, edited by T. Mura. New York: American Society of Mechanical Engineers, 1969.

Problems

10.1 One of the most powerful methods for discriminating an underground nuclear explosion from an earthquake is based on the excitation of short-period P-waves relative to long-period surface waves. If we take an explosion and a shallow earthquake that generate comparable P-waves with period around 1 s, it is observed that the Rayleigh waves generated by the explosion are an order of magnitude smaller (with period around 20 s) than those generated by the earthquake. Assume a double-couple point source for the earthquake and a point source with isotropic moment tensor for the explosion, both buried in a homogeneous half-space. Find out if the difference in source type and focal depth (the depth of an explosion cannot be greater than a few kilometers) can cause an order of magnitude difference in Rayleigh vs. P-wave excitation. If not, what other effects can account for this observation?

10.2 Some important symmetry properties for the radiation from general shear faulting on a plane surface within an infinite, homogeneous, isotropic medium can be inferred from (10.39). For shear faulting in the plane $x_3 = 0$, show that displacement components *parallel* to the fault plane are *odd* functions of distance x_3 from the fault and that the displacement *normal* to the fault is an *even* function of x_3. Hence, for traction on planes parallel to Σ at distance x_3, show that the normal component is an odd function of x_3 and that the shear components are even. Finally, show that the normal component of traction on a planar fault (in an infinite, homogeneous, isotropic medium) cannot be changed by any shearing event on the fault.

10.3 Equation (10.41) amounts to a dynamic boundary condition for tractions on the fault plane. Where do we take this condition into account in setting up a representation of the solution, such as (10.39)? Verify that this representation of the radiated field does indeed have continuity of shear stress across the fault (use results of Problem 10.2).

10.4 The opening of a crack may be represented by a displacement discontinuity $[\mathbf{u}]$ that is parallel to ν, the fault normal. Obtain the equivalent body force in an isotropic elastic body, and find the far-field body waves (P and S) in an infinite homogeneous medium (cf. equation (10.6)).

10.5 Show that the source spectrum for a faulting episode, derived from the far-field displacement as discussed in Section 10.1.4 in the limit of low frequencies, is flat at the origin ($\omega = 0$). (This result is true, whether the spectrum has a maximum at the origin, or whether there is overshoot.)

10.6 Under the assumptions of shear faulting on a plane, and slip everywhere in the same direction, we have seen that the far-field pulse shape is given by (10.13) provided fault length L, wavelength λ, and source–receiver distance r_0 satisfy the constraint $L^2 \ll \frac{1}{2}\lambda r_0$. Far-field pulse shapes for P-waves and S-waves radiate out to every direction on the focal sphere. Suppose that the pulse shape $\Omega(t)$ is radiated as an S-wave in some direction $\boldsymbol{\gamma}_S$.

a) Show that it is always possible to find a direction $\boldsymbol{\gamma}_P$ in which this same pulse shape $\Omega(t)$ is radiated as a P-wave (though the arrival time will be different, and note that we are neglecting the effects of different attenuation between P- and S-waves).

b) What is the relationship between $\boldsymbol{\gamma}_P$ and $\boldsymbol{\gamma}_S$?

c) Given a P-wave pulse shape observed in direction $\boldsymbol{\gamma}_P$, show that it is *not* always possible to find a direction in which this same pulse shape is observed as an S-wave.

10.7 The "finiteness factor" $X^{-1} \sin X$ that appears in equations (10.20)–(10.22) is very simple, because (i) the rupture is unilateral (i.e., it proceeds from one end of the fault to the other); (ii) it has constant rupture velocity; (iii) the fault width W is very small; and (iv) the slip function at each point of the fault plane is the same, apart from a delay due to the time taken for rupture to initiate.

a) Suppose that we drop assumptions (i), (ii), and (iii), but retain (iv). Show that the far-field pulse shape is then given by

$$\Omega(\mathbf{x}, \omega) = \Omega_0(\mathbf{x}, \omega) F(\boldsymbol{\gamma}, \omega),$$

where $\Omega_0(\mathbf{x}, \omega)$ is the pulse shape radiated by a point shear dislocation of strength $A \times \Delta u(\omega)$, and the finiteness factor in this more general case is

$$F(\boldsymbol{\gamma}, \omega) = \frac{1}{A} \iint_{\Sigma} \exp\, i\omega \left[\tau(\xi) - \frac{\xi \cdot \boldsymbol{\gamma}}{c} \right] d\Sigma.$$

Here A is the fault area, $\tau(\xi)$ is the time taken for the rupture to reach ξ on the fault plane, and γ is the ray direction from source to receiver.

b) In the time domain, show that $\Omega(\mathbf{x}, t)$ is given by convolving $\Omega_0(\mathbf{x}, t)$ with a pulse shape having unit "area," i.e., show that $\int_{-\infty}^{\infty} F(\gamma, t)\, dt = 1$.

c) Now drop assumption (iv) also, and show that the corresponding finiteness factor is

$$F(\gamma, \omega) = \frac{1}{M_0(\omega)} \iint_{\Sigma} \mu(\xi)\ \Delta u(\xi, \omega) \exp i\omega \left[\frac{-\xi \cdot \gamma}{c}\right] d\Sigma,$$

where $M_0(\omega) = \iint \mu(\xi) \Delta u(\xi, \omega)\, d\Sigma$. Show that this more general finiteness factor also has unit area in the time domain.